Modeling Viscoelastic Solid Earth Deformation Due To Ice Age and Contemporary Glacial Mass Changes in ASPECT

Weerdesteijn, Maaike F.M.; Naliboff, John B.; Conrad, Clinton P.; Reusen, Jesse M.; Steffen, Rebekka; Heister, Timo; Zhang, Jiaqi

Important note
To cite this publication, please use the final published version (if applicable).
Please check the document version above.

Geochemistry, Geophysics, Geosystems®

RESEARCH ARTICLE

Key Points:

- The solid Earth is deforming in response to past and present ice loading changes at rates determined by elastic and viscous parameters
- We benchmark a new viscoelastic solid Earth deformation model in the open-source code ASPECT in combination with adaptive mesh refinement
- This code can be used to study regional Earth deformation rates from ice age and contemporary ice melt on a laterally heterogeneous Earth

Correspondence to:
M. F. M. Weerdesteijn,
m.f.m.weerdesteijn@geo.uio.no

Modeling Viscoelastic Solid Earth Deformation Due To Ice Age and Contemporary Glacial Mass Changes in ASPECT

Maaike F. M. Weerdesteijn[1] , **John B. Naliboff[2]** , **Clinton P. Conrad[1]** , **Jesse M. Reusen[3]** , **Rebekka Steffen[4]** , **Timo Heister[5]**, and **Jiaqi Zhang[5]**

[1]Centre for Earth Evolution and Dynamics, University of Oslo, Oslo, Norway, [2]Department of Earth and Environmental Science, New Mexico Institute of Mining and Technology, Socorro, NM, USA, [3]Faculty of Aerospace Engineering, Delft University of Technology, Delft, The Netherlands, [4]Lantmäteriet, Gävle, Sweden, [5]School of Mathematical and Statistical Sciences, Clemson University, Clemson, SC, USA

Abstract The redistribution of past and present ice and ocean loading on Earth's surface causes solid Earth deformation and geoid changes, known as glacial isostatic adjustment. The deformation is controlled by elastic and viscous material parameters, which are inhomogeneous in the Earth. We present a new viscoelastic solid Earth deformation model in ASPECT (Advanced Solver for Problems in Earth's ConvecTion): a modern, massively parallel, open-source finite element code originally designed to simulate convection in the Earth's mantle. We show the performance of solid Earth deformation in ASPECT and compare solutions to TABOO, a semianalytical code, and Abaqus, a commercial finite element code. The maximum deformation and deformation rates using ASPECT agree within 2.6% for the average percentage difference with TABOO and Abaqus on glacial cycle (∼100 kyr) and contemporary ice melt (∼100 years) timescales. This gives confidence in the performance of our new solid Earth deformation model. We also demonstrate the computational efficiency of using adaptively refined meshes, which is a great advantage for solid Earth deformation modeling. Furthermore, we demonstrate the model performance in the presence of lateral viscosity variations in the upper mantle and report on parallel scalability of the code. This benchmarked code can now be used to investigate regional solid Earth deformation rates from ice age and contemporary ice melt. This is especially interesting for low-viscosity regions in the upper mantle beneath Antarctica and Greenland, where it is not fully understood how ice age and contemporary ice melting contribute to geodetic measurements of solid Earth deformation.

Plain Language Summary Mass changes on the Earth's surface, for example, from melting ice sheets or sea level rise, cause deflections of Earth's surface as interior rocks deform and flow. Scientists have developed models of the interior deformation resulting from loads applied to Earth's surface. Such models depend on the viscous and elastic properties of interior rocks, which quantify their capacity to deform and flow. However, because the Earth is heterogeneous, its viscoelastic properties exhibit large lateral variations that have proven difficult to accommodate within a (numerical) model. Here, we present and benchmark a new application of the open-source code in ASPECT (Advanced Solver for Problems in Earth's ConvecTion), which was originally designed to model mantle convection occurring on timescales of millions of years or longer. The ASPECT code makes use of modern numerical methods, such as adaptive mesh refinement and advanced solver techniques. In particular, we show that this code is accurate and useful for modeling solid Earth deformation occurring on timescales relevant to contemporary (in response to climate change) and ice age melting (from decades to millennia). This code is especially useful for studying regions with both past and present ice melt and a heterogeneous Earth structure, such as Greenland and Antarctica.

1. Introduction

Glacial isostatic adjustment (GIA) is the ongoing response of the solid Earth and the geoid to past and present changes in ice and ocean loading and produces solid Earth ground motion and mass redistributions. The solid Earth ground motion can be measured using GNSS (Global Navigation Satellite Systems) and the solid Earth mass displacements using ground-based gravimetry and satellite gravimetry, such as GRACE (Gravity Recovery and Climate Experiment). These geodetic measurements capture the ongoing response of the solid Earth to changes from both past (i.e., ice age) and contemporary ice load changes. Near areas of past and current ice cover, it is commonly thought that solid Earth ground motion results from a combination of (a) a viscous response to past ice load changes, and (b) an elastic response to contemporary ice load changes. Consequently, these

geodetic measurements are either (a) corrected for the viscous response to past ice load changes, based on GIA modeling, and the remaining (assumed elastic) signal is used to constrain contemporary ice load changes (e.g., Bevis et al., 2012; Simpson et al., 2011; The IMBIE Team, 2018, 2019) or (b) corrected for the elastic response to contemporary ice load changes and the remaining viscous signal is used to constrain Earth material properties (Scheinert et al., 2021, and references therein), such as mantle viscosity and lithospheric thickness, or ice sheet histories, also using GIA models.

To correct geodetic data for the viscous response to past ice load changes, GIA models commonly assume a radially symmetric Earth structure (1D) (e.g., Ivins et al., 2013; Roy & Peltier, 2018; Whitehouse et al., 2012) as opposed to a laterally heterogeneous Earth structure (3D) (e.g., Bagge et al., 2021; Li et al., 2020; H. Steffen et al., 2006; Wu et al., 1998; Yousefi et al., 2021), and yet the Earth is characterized by lateral heterogeneities. There are indications of low-viscosity mantle or weakened lithosphere underneath Antarctica and Greenland (areas characterized by both past and contemporary ice load changes), as inferred using a variety of geophysical observations, such as seismic, magnetic, and gravity data (Celli et al., 2021; Lloyd et al., 2020; Martos et al., 2018; Pappa et al., 2019; R. Steffen et al., 2018). In the presence of a low-viscosity region in the mantle, contemporary ice load change generates not only an instantaneous elastic response but can also generate a viscous response on short timescales (Weerdesteijn et al., 2022; Whitehouse, 2018). Recent studies have explored this rapid viscous response for Antarctica (Barletta et al., 2018; Bradley et al., 2015; Nield et al., 2014; Samrat et al., 2020, 2021; Wolstencroft et al., 2015; Zhao et al., 2017) and Greenland (Adhikari et al., 2021; Khan et al., 2016; Milne et al., 2018; Simpson et al., 2011; van Dam et al., 2017). The rapid viscous response is mixed with the elastic and long-term viscous deformation components of GIA, making it difficult to distinguish between solid Earth deformation due to past and contemporary ice load changes (Whitehouse, 2018). The effect of lateral viscosity variations on solid Earth deformation (Kaufmann et al., 1997; Sabadini & Portney, 1986) and whether a 3D Earth can be represented by 1D models for glacial cycle timescales (Blank et al., 2021; Marsman et al., 2021; Milne et al., 2018; van der Wal et al., 2013, 2015) and contemporary ice melt timescales (Powell et al., 2020) has been a long-standing question. Furthermore, recent efforts showed the need for 3D modeling to predict solid Earth deformation rates due to contemporary ice load changes near confined low-viscosity regions (Weerdesteijn et al., 2022).

In order to isolate the solid Earth deformation due to past or contemporary ice load changes, we need a modeling tool that functions from glacial cycle to decadal timescales. Furthermore, this tool needs to be able to manage large lateral heterogeneities in material properties (most importantly viscosity). Benchmark studies have been undertaken for viscoelastic solid Earth deformation models (Martinec et al., 2018; Spada et al., 2011). There are currently models that scale well for parallel computing (e.g., Latychev et al., 2005) or use regional mesh refinement (e.g., Blank et al., 2021; Wan et al., 2022). However, there are only few models that can manage large lateral viscosity variations, are open-source, and are built for high performance parallel computing. These are CitComSVE (Zhong et al., 2022) and Elmer (Zwinger et al., 2020), although the latter is not benchmarked on glacial cycle timescales.

In this study, we present a new open-source viscoelastic solid Earth deformation model in ASPECT (Advanced Solver for Problems in Earth's ConvecTion). This new model can be used for regional modeling but not for global studies, as it does not take into account gravity field changes induced by the deformation and does not solve for the gravitationally self-consistent redistribution of ocean water. ASPECT is an open-source finite element code to simulate problems in thermal convection in the Earth's mantle with large lateral variations in viscosity. We use ASPECT v2.4.0 (Bangerth et al., 2022a, 2022b; Clevenger & Heister, 2021; Heister et al., 2017; Kronbichler et al., 2012; Rose et al., 2017) published under the GPL2 license and builds on the deal.II v9.4 finite element library (Arndt et al., 2022). We compare solid Earth deformation using ASPECT to solutions using TABOO, a semianalytical code based on the normal mode method, and Abaqus, a commercial finite element code. A big advantage of ASPECT over other codes is that it uses modern numerical methods, such as adaptive mesh refinement (AMR) (demonstrated in Sections 5.1 and 5.2) and is built for parallel computing, also in combination with dynamically changing meshes. ASPECT can be extended by users and is under continuous development.

2. Numerical Model

ASPECT is a code to model convection processes in the Earth's mantle and is used for studies on, for example, subduction zone dynamics, dynamic topography, gravity field anomalies, and mantle plume dynamics (e.g.,

Austermann et al., 2017; Dannberg & Gassmöller, 2018; Glerum et al., 2018; Root et al., 2022). In the following sections, we describe the constitutive equations used in ASPECT and how they are modified for the purpose of modeling solid Earth deformation. We also discuss the applied boundary conditions and solvers used for our purposes.

2.1. Constitutive Equations

ASPECT solves a system of equations that describes viscous fluid motion driven by gravitational force differences. The compressible momentum (Equation 1) and continuity equations (Equation 2), also known as the compressible Stokes equations, are as follows:

$$-\nabla \cdot \left[2\eta \left(\dot{\epsilon}(\mathbf{u}) - \frac{1}{3}(\nabla \cdot \mathbf{u})\mathbf{1} \right) \right] + \nabla p = \rho \mathbf{g} \tag{1}$$

$$\nabla \cdot (\rho \mathbf{u}) = 0 \tag{2}$$

where η is the viscosity, $\dot{\epsilon}$ the strain rate, $\mathbf{u}$ the velocity, p the total pressure, ρ the density, $\mathbf{g}$ the gravity vector, and $2\eta \left(\dot{\epsilon}(\mathbf{u}) - \frac{1}{3}(\nabla \cdot \mathbf{u})\mathbf{1} \right)$ represents the deviatoric stress τ.

For solid Earth deformation modeling purposes, ASPECT solves the 3D Stokes equations assuming isothermal flow, the Boussinesq approximation, and incompressibility. Since incompressible flow with a linear rheology is modeled, the temperature equation (i.e., energy conservation equation) and updates to the viscoelastic stresses are decoupled from the momentum and continuity equations. Note that assuming incompressibility can reduce present-day uplift rates by up to a few percent (A et al., 2013), and that horizontal velocities from incompressible GIA models are not accurate due to the neglect of material dilatation. For solid Earth deformation modeling, we consider isothermal flow (i.e., constant temperature throughout the domain) and therefore we do not solve for the temperature equation. The Boussinesq approximation assumes that density variations are so small that they can be neglected, apart from the right-hand side of the momentum equation (Equation 1). Under this approximation the continuity equation (Equation 2) reduces to the following equation:

$$\nabla \cdot \mathbf{u} = 0 \tag{3}$$

The same approximation to the continuity equation is obtained when incompressible flow is assumed. Furthermore, the deviatoric stress reduces to $2\eta\dot{\epsilon}(\mathbf{u})$ for incompressible flow, and thus the momentum equation becomes the following equation:

$$-\nabla \cdot [2\eta\dot{\epsilon}(\mathbf{u})] + \nabla p = \rho \mathbf{g} \tag{4}$$

Force terms are added on the right-hand-side of the momentum equation to account for the linear viscoelastic behavior (Section 2.2) and boundary traction (Section 2.3). For incompressible and isothermal flow, under the Boussinesq approximation, the momentum (Equation 4) and continuity equations (Equation 3) reduce to the following equations:

$$-\nabla \cdot [2\eta_{\text{eff}}\dot{\epsilon}(\mathbf{u})] + \nabla p = \rho \mathbf{g} + \nabla \cdot F_{\text{e}} + \nabla \cdot F_{\text{t}} \tag{5}$$

$$\nabla \cdot \mathbf{u} = 0 \tag{6}$$

where η_{eff} is the effective, assumed Newtonian, viscosity, F_{e} the elastic force term, and F_{t} the boundary traction force term.

2.2. Viscoelastic Rheology

The viscoelastic rheology is implemented through an elastic force term and an effective viscosity in the momentum equation (Equation 5) that account for the elastic and viscous deformation mechanisms. This approach, which starts from a viscous approximation, is standard within the long-term geodynamics community (e.g., Moresi et al., 2003). Our methodology for modeling viscoelasticity in ASPECT follows the approach of Moresi et al. (2003), as outlined in Sandiford et al. (2021). Within a time step, the viscoelastic stresses are first updated using the strain rate and material properties from the previous time step. Second, the values of the viscoelastic

stresses stored on the compositional fields are simultaneously advected and updated via a reaction term in the advection equation. Last, the updated stresses on the compositional fields are used to construct and solve the Stokes system (Equations 5 and 6) with the elastic force term and boundary traction force term (Section 2.3). We use an implicit second-order accurate time stepping scheme (BDF2 as described in Heister et al. (2017)) for the compositional fields that keeps track of the stresses, while the nonlinearity of the viscosity is linearized using a splitting approach with a single Stokes solve (see Section 2.4).

The velocity gradient tensor I^t and deviatoric stress tensor τ^t are constructed from the velocity solution and stored stress components of the previous time step t. The new viscoelastic stresses are computed according to the following equation:

$$\tau^{t+\Delta t} = \eta_{\text{eff}} \left(2\hat{D}^t + \frac{\tau^t}{\mu \Delta t} + \frac{W^t \tau^t - \tau^t W^t}{\mu} \right) \tag{7}$$

with

$$\hat{D} = \frac{1}{2} \left(I + I^T \right) \tag{8}$$

$$W = \frac{1}{2} \left(I - I^T \right) \tag{9}$$

$$\eta_{\text{eff}} = \eta \frac{\Delta t}{\Delta t + \alpha} \tag{10}$$

where superscript t and $t + \Delta t$ indicate the previous and current time step, and μ is the shear modulus describing the relation between applied force and elastic deformation. $\hat{D}$ and W are the deviatoric rate of the deformation tensor (Equation 8) and the spin tensor (Equation 9), respectively, and are a function of the velocity gradient tensor. η_{eff} is the effective viscosity (Equation 10) and is defined as a function of (material) viscosity η, time step size Δt, and shear (Maxwell) relaxation time α, where $\alpha = \eta/\mu$. In this study, we only consider linear (fixed) viscosities for each distinct compositional field. ASPECT has the option for modeling viscoelastic-plastic rheologies, with additional options for selecting dislocation creep, diffusion creep or composite viscous flow laws but has not been benchmarked yet in combination with a free surface and boundary traction. Nonlinear rheologies affect Equation 7 through a different definition (consisting of more terms) of the effective viscosity.

With the viscoelastic stresses of the previous and current time step, the reaction term for the deviatoric stress q is determined. As described above, lithologic layers and stresses are tracked on compositional fields. Compositional fields were originally intended to track the chemical composition of the convecting medium but have been shown to be useful for other purposes, such as tracking materials, simulating phase changes, and tracking finite strain accumulation. For each field $c_i(\mathbf{x}, t)$, with $i = 1\ldots C$, an advection equation is solved, which updates the stresses on the field through a reaction term q:

$$\frac{\partial c_i}{\partial t} + \mathbf{u} \cdot \nabla c_i = q_i \tag{11}$$

with

$$q = \tau^{t+\Delta t} - \tau^t \tag{12}$$

Then, the Stokes system (Equations 5 and 6) is constructed with the updated deviatoric stress and the elastic force term, which is defined as follows:

$$F_e = -\frac{\eta_{\text{eff}}}{\eta_e} \tau^{t+\Delta t} \tag{13}$$

where η_e is the "elastic" viscosity and equals $\mu \Delta t$. A new velocity field is determined by solving the Stokes system.

2.3. Boundary Conditions

In this study, to allow for surface deformation, we use a free surface on the top boundary (i.e., the Earth's surface) (Rose et al., 2017). The free surface is defined as having zero normal stress on the boundary. Thus, the following

condition must be satisfied: $\sigma \cdot \mathbf{n} = 0$, where $\mathbf{n}$ is the vector normal to the boundary and $\sigma = 2\eta_{\text{eff}}\dot{\epsilon}(\mathbf{u})$ being the total stress (i.e., the total stress is equal to the deviatoric stress since there is no pressure gradient at the top surface). When there is flow across the boundary, the mesh must be able to deform to satisfy the above condition. On the free surface, mesh velocity $\mathbf{u}_m$ is calculated as follows:

$$\mathbf{u}_m = (\mathbf{u} \cdot \mathbf{n})\mathbf{n} \tag{14}$$

Using this approach, the Eulerian advection terms need to be corrected for the mesh velocity. The momentum and continuity equations become the following equations:

$$-\nabla \cdot [2\eta_{\text{eff}}\dot{\epsilon}(\mathbf{u} - \mathbf{u}_m)] + \nabla p = \rho\mathbf{g} + \nabla \cdot F_e + \nabla \cdot F_t \tag{15}$$

$$\nabla \cdot (\mathbf{u} - \mathbf{u}_m) = 0 \tag{16}$$

Furthermore, a quasi-implicit integration scheme is used to dampen free surface position instabilities arising from small deviations in the free surface location (Rose et al., 2017).

Next to the free surface on the top boundary, we also apply a traction force to represent the surface ice loading. The ice loading is a known external force, resulting in an unknown velocity. The given pressure is applied as a force that is normal to the boundary. The lateral and bottom boundaries are free-slip boundaries. A free-slip boundary requires that the flow is tangential to the boundary, that is, $\mathbf{u} \cdot \mathbf{n} = 0$. The boundary traction is represented as F_t in the momentum equation (Equation 5).

2.4. Solver Options

The solution of the Stokes system can be obtained using an algebraic multigrid (AMG) solver or a matrix-free geometric multigrid (GMG) solver. While the AMG solver can solve problems on the order of ~0.5–1.0 billion degrees of freedom (DoF) and scale efficiently on up to ~5,000 cores, the GMG solver can solve significantly larger problems, efficiently scaling to ~100,000 cores, and reduce memory consumption by up to a factor of 8 (Clevenger et al., 2020; Clevenger & Heister, 2021). Here, we take advantage of recent development work in ASPECT (Bangerth et al., 2022b) integrating the GMG solver with mesh deformation and elasticity, which speeds up our simulations significantly (see Section 6). Notably, the use of the GMG solver requires element-wise averaging of the viscosity, but we found this has no noticeable effect on accuracy for a given resolution.

Three different nonlinear solving schemes can be applied for our application in the model setup. The first option is "single Advection, single Stokes" in which only one nonlinear iteration is done, that is, the compositional fields and Stokes system are solved once per time step. The second option, the "iterated Advection and Stokes" scheme iterates this decoupled approach by alternating the solution of the composition and Stokes system. The third option is "single Advection, iterated Stokes" in which the composition equation is solved once at the beginning of each time step and then iterates over the Stokes system. We experienced no improvement of free surface deformation accuracy by applying an iterated Stokes and/or iterated advection scheme. This finding is consistent for a linear and incompressible system, under the condition that the time step size and solver tolerance are sufficiently small. Thus, for computational efficiency, we use the "single Advection, single Stokes" solver scheme. The solver schemes required for a nonlinear rheology are "single Advection, iterated Stokes" or "iterated Advection and Stokes." The former *solver scheme* is most commonly used but theoretically iterating on both the advection and Stokes system each time step is more accurate as the fields (composition, temperature) updated during advection steps are contained within the rheological formulation.

3. Benchmark Study: Short and Long Timescales

Two benchmark tests are executed to validate the performance of the solid Earth deformation implementation in ASPECT with respect to two reference GIA/solid Earth deformation modeling codes, TABOO and Abaqus. Both reference codes were part of the benchmark study by Spada et al. (2011). All models use a layered Earth structure and are forced with a time-dependent surface loading. The two benchmark tests are the solid Earth deformation in response to short timescale (contemporary ice melt) and long timescale (glacial cycle) surface loading changes. The reference models and the test setup are described in the following sections.
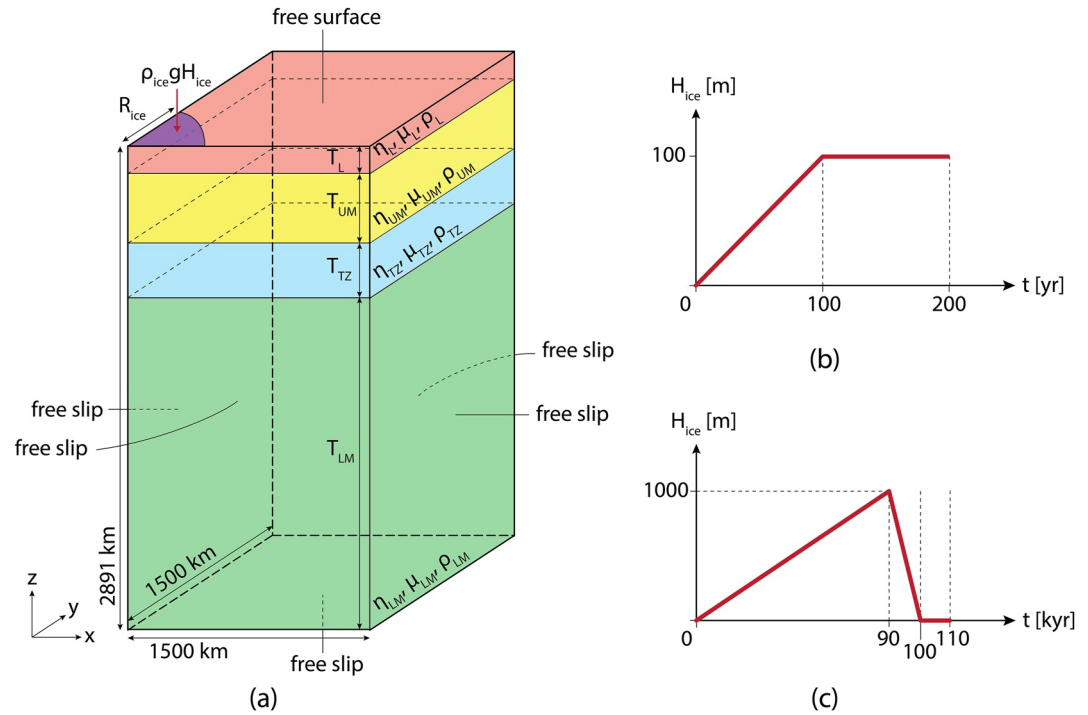
Figure 1. (a) The box model geometry (not to scale) in ASPECT with lithosphere (red), upper mantle (yellow), transition zone (blue), lower mantle (green), boundary traction from ice loading (purple), boundary conditions, and layer material properties. (b) The ice loading height as a function of time for the short timescale simulation (contemporary ice melt). (c) The ice loading height as a function of time for the long timescale simulation (glacial cycle).

3.1. Reference Models

TABOO is an open-source postglacial rebound calculator (Spada, 2003; Spada et al., 2003). The model assumes an Earth that is layered, nonrotating, incompressible, self-gravitating, spherically symmetric, and is using a linear Maxwell viscoelastic rheology. It computes the surface deformation resulting from a variable surface ice loading, using the normal mode method (Peltier, 1974, 1976; Vermeersen & Sabadini, 1997; Wu & Peltier, 1982). The surface ice loading can be set by the user. The Earth structure can be chosen from a preset selection or set by the user by changing the FORTRAN source code. This latter option requires caution as it involves changing average density and mass reference parameters, which are used in the computation of the surface spherical harmonics.

Abaqus is a commercial finite-element software package (Dassault Systèmes, 2019). Wu (2004) modified the equation of motion to include the restoring force of isostasy as a boundary condition, such that the code is applicable to GIA problems. In this study, we use a nonaxisymmetric box model geometry in Abaqus (Schotman et al., 2008), which is incompressible and nonself-gravitating (e.g., as in H. Steffen et al. (2006) or Wu et al. (2021)). For the lateral boundaries no horizontal displacement is allowed (free slip) and for the bottom boundary no displacement, neither vertically nor horizontally, is allowed (no slip). Material parameters can vary in all dimensions, similar to ASPECT.

3.2. Test Setup

For the benchmark tests, we use a box model geometry in ASPECT (Figure 1a) and Abaqus, and a spherical model geometry in TABOO. The Earth structure is vertically (or radially for TABOO) symmetric, since TABOO cannot include lateral variations in material properties. We apply an elastic lithosphere, and a viscoelastic upper mantle, transition zone, and lower mantle. The horizontal dimensions are 1,500 km for ASPECT and 3,000 km for Abaqus (due to nonaxisymmetry), and the vertical dimension is 2,891 km (depth of the core-mantle boundary). The horizontal dimensions are chosen such that the model geometry is sufficiently large to allow for deformation far from the load without being affected by the model lateral boundaries. The choice of horizontal dimensions

Table 1
Earth Model Properties, as in Spada et al. (2011)

Layer	Radius R (km)	Thickness T (km)	Density ρ (kg m^{-3})	Shear modulus μ (Pa)	Viscosity η (Pa s)	Gravity g (m/s^2)
Lithosphere, L	6,371	70	3,037	$0.50605 \cdot 10^{11}$	∞	9.815
Upper mantle, UM	6,301	350	3,438	$0.70363 \cdot 10^{11}$	$1 \cdot 10^{21}$	9.854
Transition zone, TZ	5,951	250	3,871	$1.05490 \cdot 10^{11}$	$1 \cdot 10^{21}$	9.978
Lower mantle, LM	5,701	2,221	4,978	$2.28340 \cdot 10^{11}$	$2 \cdot 10^{21}$	10.024
Core	3,480	3,480	10,750	0	0	10.457

is thus dependent on the size of the ice loading. The effect of the lateral boundaries on surface deformation is discussed in Appendix A.

The layer properties for the Earth model used in TABOO are given in Table 1. This Earth model has been extensively used in GIA and solid Earth deformation code benchmarks (Martinec et al., 2018; Spada et al., 2011; Zwinger et al., 2020) and is a preset Earth model in TABOO. For ASPECT we apply the following modifications: we do not model the core (the same for Abaqus), the lithospheric viscosity is set to 10^{40} Pa s to approximate an elastic lithosphere, and we use constant gravity throughout the model of 9.815 m/s^2, while TABOO and Abaqus do include the radially/vertically changing gravity.

The top boundary is a free surface, the bottom boundary and lateral boundaries are free slip. By applying the lateral free-slip boundaries (e.g., only tangential flow), and a symmetric ice loading in ASPECT, the model is axisymmetric. This means that only a quarter of the full geometry needs to be simulated, saving computational resources. Abaqus models the full ice disc as the model is not axisymmetric.

For both loading scenarios, the ice loading is a quarter disc (full disc in TABOO and Abaqus) with a spatially constant height H_{ice} (Figure 1a). The radius of the ice disc R_{ice} is 100 km, the ice density ρ_{ice} is 931 kg/m^3, and the magnitude of the gravity at the surface is 9.815 m/s^2. For the short timescale simulation the ice height linearly increases from 0 to 100 m over 100 years, that is, 1 m/yr ice height change, which is the order of magnitude for contemporary ice melt in Antarctica and Greenland (Helm et al., 2014; The IMBIE Team, 2019), after which the height remains a constant 100 m from 100 to 200 years (Figure 1b). The constant ice height is added to test the code performance in case of a change in surface loading rate. We choose a linear loading increase (ice growth) as opposed to decrease (ice melt), as the latter option would require an instantaneous loading at 0 years of 100 m, which is not realistic.

For the long timescale simulation, we approximate the ice height change over a glacial cycle of 110 kyr. The ice height linearly increases from 0 to 1,000 m over 90 kyr (glacial maximum), then linearly decreases to 0 m over 10 kyr, from 90 to 100 kyr (start interglacial period), after which the height remains a constant 0 m from 100 to 110 kyr (present day) (Figure 1c). This is a rough representation of the evolution of an ice sheet during the last glacial cycle.

For the simulations in ASPECT, we make us of a constant layered mesh through time (Figure 2). Tests with AMR are discussed in Section 5.1. The cell size (x, y, z) in the upper 100 km is 6.25 × 6.25 × 6.02 km, and 50 × 50 × 48.18 km in the rest of the model, with a transition using 12.5 × 12.5 × 12.05 km and 25 × 25 × 24.09 km sized cells. The vertical cell dimension is slightly smaller than the horizontal cell dimension as we set 30 cells in horizontal direction (1,500 km) and 60 cells in vertical direction (2,891 km) for the initial mesh. For the simulations in Abaqus the mesh is also constant through time. The horizontal resolution is 5 km close to the ice loading (a square of 400 × 400 km centered around the load), and 200 km elsewhere. The vertical resolution varies from 8.75 to 277.625 km, increasing with depth (8 elements per layer). In ASPECT, we use quadratic continuous 3D finite elements (27 nodes) for the velocity with 3 DoF per node and linear continuous 3D finite elements (8 nodes) for the pressure with 1 DoF per node. In Abaqus linear continuous 3D finite elements (8 nodes) are used with 3 DoF per node for the velocity and 1 DoF per node for the pressure. The spectral resolution in TABOO with a maximum degree of 4,096 corresponds to ∼5 km resolution. In ASPECT the time step size for the short timescale simulation is 2.5 years and for the long timescale simulation is 50 years. From trial and error we found that smaller time step sizes do not yield more accurate results.
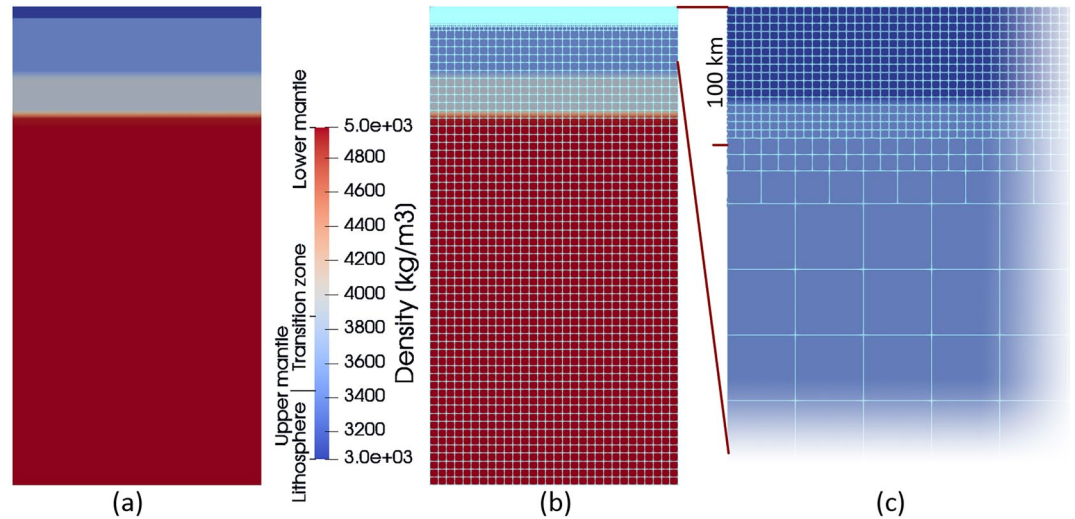
Figure 2. (a) Front view of the box geometry in ASPECT with density variations with depth. (b) Same as (a) but with overlain mesh. (c) Same as (b) but zoomed in to see the mesh cells size changing from ∼50 km to ∼6.25 km in the upper 100 km of the model.

4. Benchmark Results and Model Performance

Here, we present the benchmark results for the short timescale simulation (Section 4.1) and the long timescale simulation (Section 4.2) and a discussion on the models performances (Section 4.3).
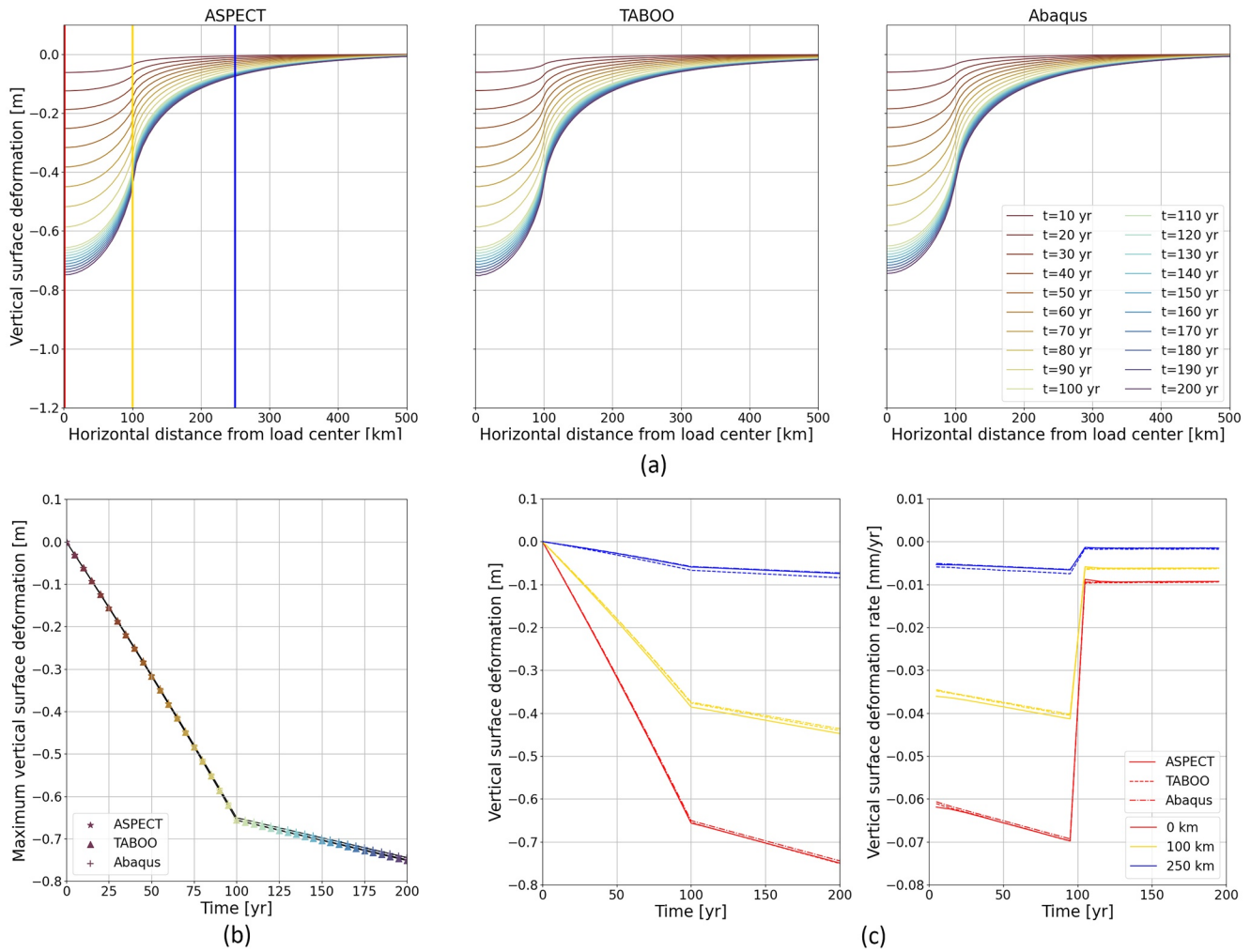
4.1. Short Timescale Simulation

The largest vertical surface deformation is, as expected, found underneath the load center, and the location of largest deformation gradient coincides with the boundary of the ice disc at 100 km distance (Figure 3a). Most deformation takes place over the first 100 years, when the ice load increases, followed by 100 years of slower surface deformation increase due to the constant loading, also visible in the abrupt kink in deformation amplitudes and rates (Figures 3b and 3c). From a first view, the deformation profiles (Figure 3a) look very similar among codes. Deviations between codes can be seen in the far field, where boundary effects may play a role for ASPECT and Abaqus (Appendix A). Furthermore, ASPECT under- or overshoots the deformation rate at times of ice loading changes, but quickly converges to the solutions from TABOO and Abaqus (Figure 3c, right). Recent testing suggests that the following components of the numerical implementation may contribute to the under- and overshoots but would require further testing to isolate the exact contributing factors: the order in which stresses are updated, the time stepping scheme (we refer to details on the "elastic" time step in Moresi et al. (2003) and Sandiford et al. (2021)) or something intrinsic to storing and advecting stresses on compositional fields. We calculate the average absolute difference and average percentage difference according to the following equations:

$$\text{average absolute difference} = \frac{\sum_n |\mathbf{a_n} - \mathbf{b_n}|}{|\mathbf{a}|} \tag{17}$$

$$\text{average percentage difference} = \frac{\sum_n (|\mathbf{a_n} - \mathbf{b_n}|)/|\mathbf{b_n}|}{|\mathbf{a}|} \cdot 100\% \tag{18}$$

where **a** and **b** are arrays with *n* elements (time steps) with the deformation or deformation rate solutions, **a** is the ASPECT solution, and **b** the TABOO or Abaqus solution. The maximum vertical surface deformation is very similar between ASPECT, TABOO, and Abaqus (Figure 3b), and the average percentage difference at the load center over 200 years is only 0.28% between ASPECT and TABOO (Table 2). For all distances from the load center (0, 100, and 250 km) the average absolute difference in deformation between ASPECT–TABOO and ASPECT–Abaqus is smaller than 0.01 m (Figure 3c, left), with the largest average percentage difference (10.64%) at 250 km between ASPECT and TABOO (Table 2). However, the deformation at 250 km is already

Figure 3. Short timescale simulations: (a) Vertical surface deformation as function of the horizontal distance from the load center along $y = x$ at different time intervals (colors) for ASPECT (left), TABOO (middle), and Abaqus (right), with vertical lines at 0 km (red), 100 km (yellow), and 250 km (blue). (b) Maximum vertical surface deformation for ASPECT (stars), TABOO (triangles), and Abaqus (pluses), with marker colors corresponding to the times in plot (a). (c) Maximum vertical surface deformation (left) and maximum vertical surface deformation rate (right) as function of time for ASPECT (solid line), TABOO (dashed line), and Abaqus (dash-dotted line) at 0 km (red), 100 km (yellow), and 250 km (blue) distance from the load center.

considerably smaller because of the distance from the load (−0.075 m at 250 km as opposed to −0.75 m underneath the load center after 200 years). For the deformation rate, we see constant deviations until the end of the load increase at 100 years, after which the solutions for ASPECT and TABOO are within 0.0003 mm/yr from each other at 200 years (Figure 3c, right). The largest average percentage difference in deformation rate are found at 250 km (Table 2). Again, the deformation rate is considerably smaller at 250 km compared to 100 and 0 km (underneath the load center). The average percentage difference in deformation and deformation rate between ASPECT and Abaqus at 250 km, 2.25% and 2.30%, respectively, are much smaller than compared to TABOO (Table 2), which suggests this is due to the influence of the lateral boundaries (Appendix A) or sphericity and self-gravitation (Appendix B). Overall, underneath the load center, we see average percentage differences of deformation and deformation rates between ASPECT–TABOO and ASPECT–Abaqus within 1.4% of each other and within 3.0% at the load boundary at 100 km distance.

4.2. Long Timescale Simulation

The vertical surface deformation in the long timescale simulation is larger than in the short timescale simulation because of the 10 times larger maximum ice height. The deformation increases up to 90 kyr, after which it decreases drastically (Figure 4), which is consistent with the change in applied surface loading. The maximum

Table 2
Average Absolute and Percentage Difference of Vertical Surface Deformation and Deformation Rate at Different Distances From the Load Center Between ASPECT and TABOO and ASPECT and Abaqus for the Short Timescale Simulation

	ASPECT–TABOO			
	Deformation		Deformation rate	
Distance from load center (km)	Avg. absolute difference (m)	Avg. percentage difference (%)	Avg. absolute difference (mm/yr)	Avg. percentage difference (%)
0	0.0009	0.28	$2.01 \cdot 10^{-4}$	1.38
100	0.0062	2.25	$5.60 \cdot 10^{-4}$	2.66
250	0.0061	10.64	$4.90 \cdot 10^{-4}$	11.47
	ASPECT–Abaqus			
	Deformation		Deformation rate	
Distance from load center (km)	Avg. absolute difference (m)	Avg. percentage difference (%)	Avg. absolute difference (mm/yr)	Avg. percentage difference (%)
0	0.0041	0.91	$3.38 \cdot 10^{-4}$	0.84
100	0.0083	2.92	$6.06 \cdot 10^{-4}$	1.95
250	0.0009	2.25	$8.41 \cdot 10^{-5}$	2.30

vertical surface deformation is very similar between ASPECT, TABOO, and Abaqus (Figure 4b). ASPECT models a slightly larger maximum surface deformation (−64.5 m) than TABOO (−63.8 m) and Abaqus (−63.5 m) at the ice height maximum at 90 kyr (Figure 4b) and also after 110 kyr, −10.8 m for ASPECT, −9.7 m for TABOO, and −9.9 m for Abaqus. The average percentage difference over 110 kyr is less than 1.3% for both the deformation and deformation rate at 100 km distance and underneath the load center between ASPECT and TABOO and less than 2.8% between ASPECT and Abaqus (Table 3). Again, the largest difference between ASPECT and TABOO we see further away from the ice load at 250 km distance (Figure 4c, blue lines, and Table 3). Also for the long timescale simulation, the average percentage difference in deformation and deformation rate between ASPECT and Abaqus at 250 km, 2.29% and 3.72% respectively, is much smaller than compared to TABOO (Table 3). Overall, underneath the load center, we see average percentage differences of deformation and deformation rates between ASPECT–TABOO and ASPECT–Abaqus within 2.6% of each other and within 2.8% at the load boundary at 100 km distance. The deformation and deformation rate differences between the models are consistent for the short and long timescale simulations.

4.3. Model Performance

The deformation solutions do not perfectly agree due to model differences, which will be discussed here. As mentioned earlier, the mesh resolution, both vertically (or radially) and horizontally (or laterally) varies for each model. An increase in consistency in model meshes is expected to improve model comparisons. Furthermore, TABOO is fully spherical, while ASPECT and Abaqus are box models and have lateral boundaries. The lateral boundaries are closed (e.g., no material inflow and outflow), which causes material to move vertically along these boundaries. To minimize this effect, it is important to choose a large model horizontal dimension with respect to the load size (Appendix A). Moreover, TABOO is self-gravitating, whilst ASPECT and Abaqus are nonself-gravitating. Amelung and Wolf (1994) and Wu and Johnston (1998) compared surface deformation following ice age loading for a spherical Earth and a nonspherical Earth approximation and showed that the effects of sphericity and self-gravitation partly cancel each other out. They found that surface deformation results are sufficiently accurate with a nonspherical Earth approximation for Fennoscandian-sized ice sheets and also for Laurentide-sized ice sheets but the nonspherical Earth approximation accuracy decreases in the periphery of the ice sheet. Ivins and James (1999) showed similar results and found sufficiently accurate results (generally ~1% difference, and ~10% in the periphery between spherical and nonspherical Earth) for ice sheets up to 20° in size. We show comparable results between ASPECT and TABOO for wider surface loads (Appendix B), making ASPECT suitable for regional solid Earth deformation modeling. Also, for model horizontal dimensions larger than 1,500 km for the numerical models, we see an additional small deviation (<1%) compared to TABOO (see Appendix A), which will affect percentage deviations. In ASPECT, we use constant gravity within the 3D box geometry, but TABOO and Abaqus employ variable gravity. As most material movement following ice loading changes takes place in the upper mantle,
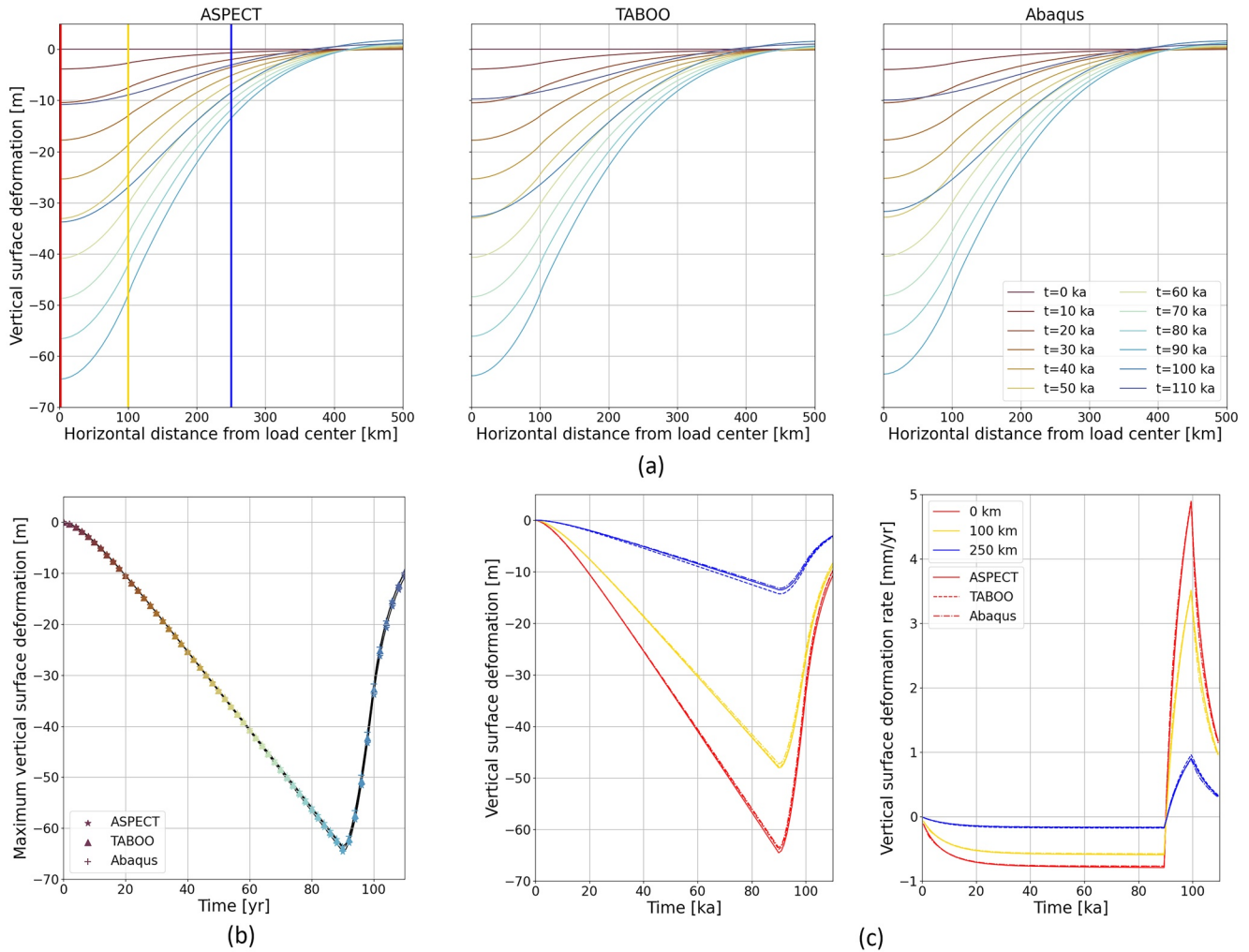
Figure 4. Long timescale simulations: (a) Vertical surface deformation as function of the horizontal distance from the load center along $y = x$ at different time intervals (colors) for ASPECT (left), TABOO (middle), and Abaqus (right), with vertical lines at 0 km (red), 100 km (yellow), and 250 km (blue). (b) Maximum vertical surface deformation for ASPECT (stars), TABOO (triangles), and Abaqus (pluses), with marker colors corresponding to the times in plot (a). (c) Maximum vertical surface deformation (left) and maximum vertical surface deformation rate (right) as function of time for ASPECT (solid line), TABOO (dashed line), and Abaqus (dash-dotted line), at 0 km (red), 100 km (yellow), and 250 km (blue) distance from the load center.

we do not expect a significant effect of the constant gravity assumption on the solid Earth deformation solution as gravity reduces by only 1.7% from the surface to the bottom of the transition zone (Table 1). Lastly, ASPECT uses quadratic finite elements, while Abaqus uses linear elements. Quadratic elements improve accuracy as they deform more realistically and capture more geometric detail with fewer elements. Generally, despite these differences, the models show a very good agreement, which gives confidence in the performance of our new solid Earth deformation model in ASPECT.

5. Benchmark Variations: Adaptive Mesh Refinement and Lateral Heterogeneous Viscosity

In this section, we apply changes to the original short timescale benchmark test to demonstrate the use of AMR in ASPECT (Section 5.1), and we demonstrate that ASPECT can manage large lateral viscosity variations in combination with an adaptive mesh (Section 5.2).

5.1. Adaptive Mesh Refinement

Here, we demonstrate the use of AMR for GIA/solid Earth deformation studies. Adaptive mesh refinement has the advantage of using a different regionally refined mesh at every time step. This is especially useful for Antarctica,

Table 3
Average Absolute and Percentage Difference of Vertical Surface Deformation and Deformation Rate at Different Distances From the Load Center Between ASPECT and TABOO for the Long Timescale Simulation

	ASPECT–TABOO			
	Deformation		Deformation rate	
Distance from load center (km)	Avg. absolute difference (m)	Avg. percentage difference (%)	Avg. absolute difference (mm/yr)	Avg. percentage difference (%)
0	0.327	1.21	$1.11 \cdot 10^{-2}$	1.11
100	0.137	0.79	$6.58 \cdot 10^{-3}$	0.78
250	0.381	5.80	$1.28 \cdot 10^{-2}$	5.82
	ASPECT–Abaqus			
	Deformation		Deformation rate	
Distance from load center (km)	Avg. absolute difference (m)	Avg. percentage difference (%)	Avg. absolute difference (mm/yr)	Avg. percentage difference (%)
0	0.526	1.95	$3.13 \cdot 10^{-2}$	2.52
100	0.420	1.93	$2.36 \cdot 10^{-2}$	2.71
250	0.157	2.29	$8.10 \cdot 10^{-3}$	3.72

where in some areas most of the ice history is not well constrained for older times and ice history resolution is increased for more recent times. These areas could be modeled with a coarse resolution when the ice history is not well constrained and with a more refined mesh resolution at times of higher resolution ice history. This allows for faster computation of the entire loading history.

In order to use ASPECT's AMR capabilities in combination with a free surface, we need to apply a constant density throughout the domain. With a laterally varying mesh, the vertically varying density is not equally represented laterally and free surface instabilities arise. In Appendix C we analyze the model performance with a constant density instead of a density profile without AMR and the effect of the density magnitude on surface deformation. However, glacially induced stresses largely depend on the density distribution (see the equations in Wu (2004)) and an increased density for the crust would result in enlarged and inaccurate stresses. To test AMR, we set the constant density equal to the volume-averaged mantle density of the Earth model density profile, 4491.76 kg/m^3. ASPECT's mesh refinement criterion is based on the strain rate norm at the center of each cell. The cells with the smallest error in strain rate norm, accounting for 5% of the total error, are flagged for coarsening, and the cells with the largest error, accounting for 30% of the total error, are flagged for refinement at each time step. With the AMR functionality, ASPECT balances the solution accuracy and computational resources for the simulation. The size of the near cubical cells varies between 50 and 6.25 km (Figure 5).
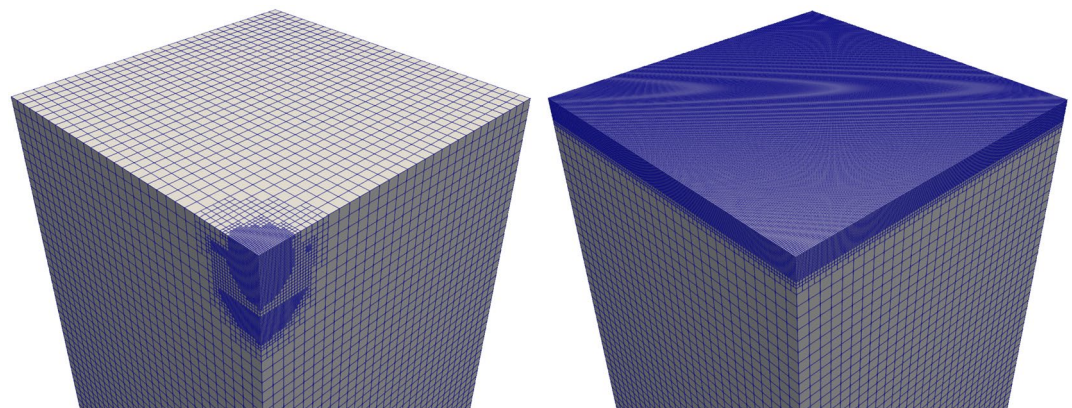
Figure 5. (left) The mesh at 200 years with adaptive mesh refinement and (right) with a constant layered mesh through time, with cell sizes ranging between ~50 and ~6.25 km.
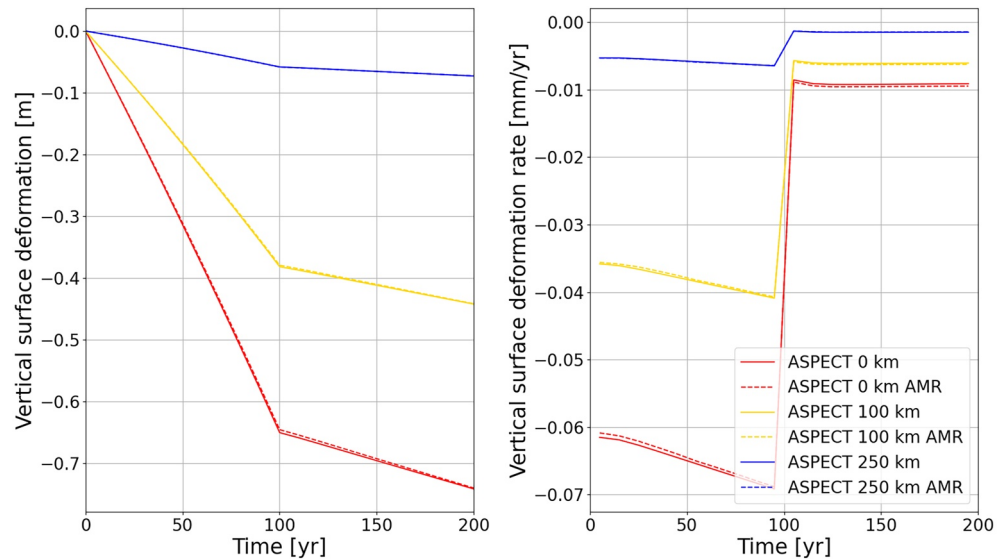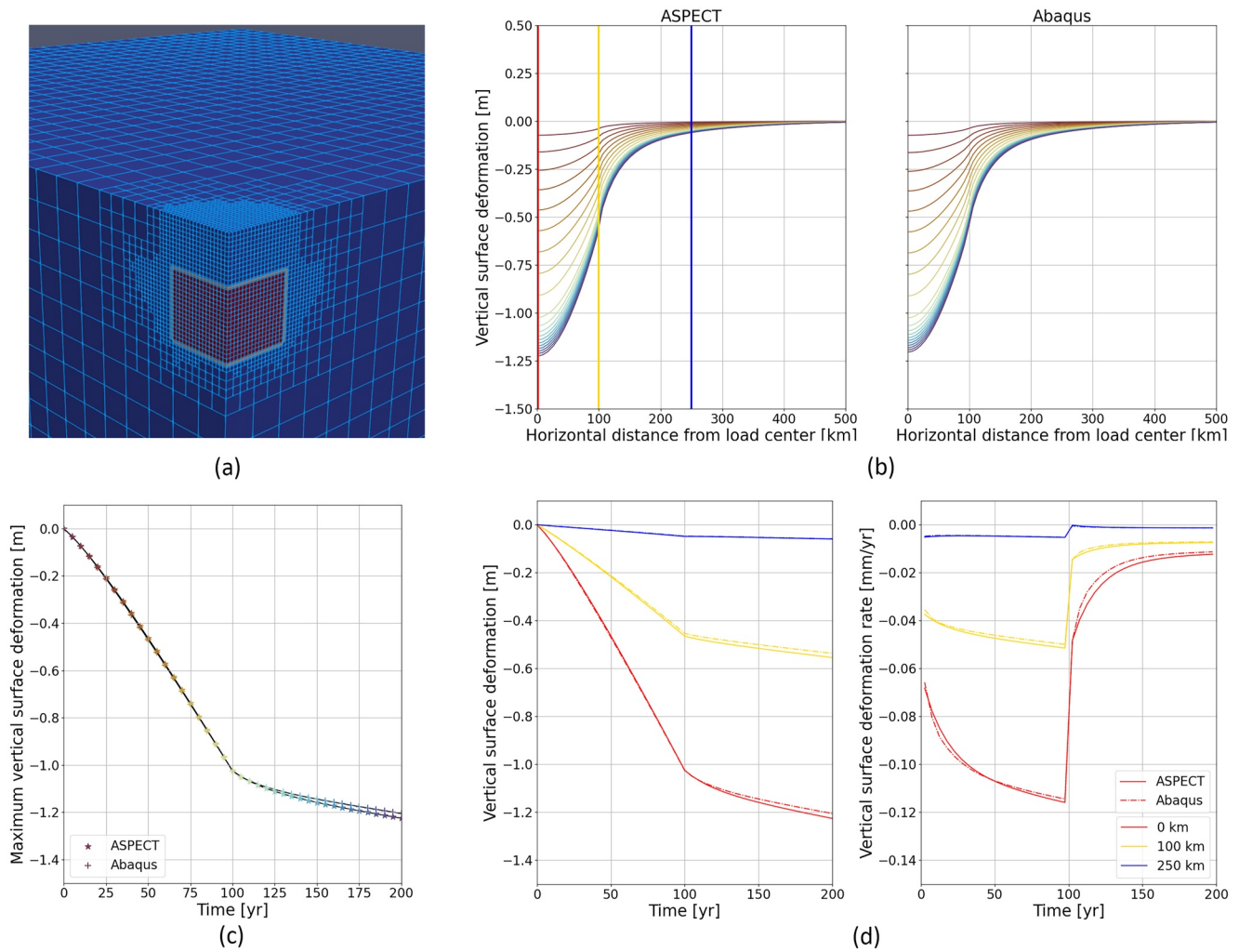
Figure 6. Maximum vertical surface deformation (left) and rate (right) as function of time for ASPECT with the constant layered mesh (solid line), and ASPECT with the adaptively refined mesh (adaptive mesh refinement) (dashed line), at 0 km (red), 100 km (yellow), and 250 km (blue) distance from the load center.

The difference in vertical surface deformation and deformation rates between the constant layered mesh and the adaptive mesh is small (Figure 6) and of the same order as the differences between ASPECT–TABOO and ASPECT–Abaqus (Figure 3). The constant layered mesh simulation takes 74 min 14 s (~111 million DOF), and the AMR simulation takes 63 min and 32 s (~9 million DOF), ~15% faster (on 512 CPU). The largest differences in computation time come from the speed-up of building the Stokes and composition systems (fewer cells and thus fewer integration points for the adaptively refined mesh) and the slowdown associated with redefining the mesh structure. We refine the mesh every time step, which is expensive. The runtime can be further reduced by doing the AMR during fewer steps and by optimizing the AMR criteria based on strain rate when no boundary traction is present at time zero (the mesh starts out refined, ~113 million DOF, and focuses onto areas with active boundary tractions in the following time steps). We recommend using AMR for solid Earth deformation applications because of the potentially considerable speedup of the simulation while maintaining the same accuracy of the solution compared to using a constant mesh through time.

5.2. Lateral Heterogeneous Viscosity

The Earth is laterally heterogeneous, and therefore there is a need for solid Earth deformation and GIA codes that can include lateral variations in Earth material properties. Here, we demonstrate the code performance in the presence of a low-viscosity region underneath the ice load, in combination with AMR. We use the same Earth model as in the previous section but include a (quarter) cylindrical shaped low-viscosity region underneath the ice load. The low-viscosity region radius is 100 km, the viscosity is $1 \cdot 10^{19}$ Pa s, the upper depth is 70 km (boundary between upper mantle and lithosphere), and the lower depth is 170 km (thickness is 100 km). We compare ASPECT with Abaqus, as TABOO cannot include lateral variations in material properties. The constant density is 4,491.76 kg/m^3 and the shear modulus of the low-viscosity region remains equal to that of the upper mantle (70.363 GPa). The refinement criteria are the same as in the previous test: the cells with the smallest error in strain rate norm, accounting for 5% of the total error, are flagged for coarsening, and the cells with the largest error, accounting for 30% of the total error, are flagged for refinement at each time step.

The mesh is refined based on the strain rate and shows a finer refinement at the location of the surface load and the low-viscosity region, where material flows faster than elsewhere (Figure 7a). Due to the low-viscosity region, for the same loading scenario, the maximum vertical surface deformation (−1.23 m, Figure 7c) is larger than for the layered solution (−0.75 m, Figure 3b). The deformation profiles of ASPECT and Abaqus look similar (Figure 7b) but on closer inspection the maximum vertical surface deformation solutions do deviate (Figure 7c) with an average percentage difference of 1.18% (Table 4). Generally, the ASPECT deformation and deformation

Figure 7. Low-viscosity region short timescale simulations: (a) the mesh in ASPECT after 200 years (light blue) with the low-viscosity region (red). (b) Vertical surface deformation as function of the horizontal distance from the load center along $y = x$ at different time intervals (colors) for ASPECT (left) and Abaqus (right), with vertical lines at 0 km (red), 100 km (yellow), and 250 km (blue). (c) Maximum vertical surface deformation for ASPECT (stars) and Abaqus (pluses), with marker colors corresponding to the times in plot (b). (d) Maximum vertical surface deformation (left) and maximum vertical surface deformation rate (right) as function of time for ASPECT (solid line) and Abaqus (dash-dotted line), at 0 km (red), 100 km (yellow), and 250 km (blue) distance from the load center.

Table 4
Average Absolute and Percentage Difference of Vertical Surface Deformation and Deformation Rate at Different Distances From the Load Center Between ASPECT and Abaqus for the Short Timescale Simulation With a Low-Viscosity Region

Distance from load center (km)	Deformation		Deformation rate	
	Avg. absolute difference (m)	Avg. percentage difference (%)	Avg. absolute difference (mm/yr)	Avg. percentage difference (%)
0	0.009	1.18	$1.91 \cdot 10^{-3}$	8.05
100	0.010	2.71	$8.71 \cdot 10^{-4}$	4.70
250	0.001	2.30	$1.30 \cdot 10^{-4}$	8.37

rate is larger than the Abaqus solution. The average percentage difference for the deformation is within 2.8% for all distances. The deformation rate shows larger deviations, up to 8.4%.

Here, we illustrate some of the reasons that the codes provide similar but different solutions in the presence of a lateral viscosity jump. Previously ASPECT and Abaqus runs utilized the same density profile. Here, we use an adaptive mesh which requires a constant density throughout the domain in combination with the free surface. The constant density results in a maximum difference of 2.7% for the deformation and deformation rate over all distances with respect to the density profile (Appendix C). Furthermore, ASPECT uses quadratic elements for the velocity and linear elements for the pressure, whereas in the Abaqus simulations, linear elements are applied. In ASPECT, on the boundary of the low-viscosity region, the viscosity value is interpolated between the values inside and outside the low-viscosity region, resulting in a linear change of the viscosity over an element (possible due

to the quadratic element with nodes in the center of the vertices). This is not only true for the lateral extent of the low-viscosity region but also for the thickness and the spatial representation of the layers with depth. The difference in the order of the elements comes with a slightly different representation of the Earth model but of course also a change in computational resources. The simulation in ASPECT takes 55 min and 0 s on 256 CPU, whereas the simulation in Abaqus takes 514 min and 59 s on 16 CPU, which is ~1.7 times faster than ASPECT when dividing the ASPECT run time by 16 to normalize the number of CPUs used (note that ASPECT only models a quarter of the geometry due to axisymmetry). Abaqus is commercial software that is highly optimized for (elastic) deformation problems, and thus it is no surprise that Abaqus runs faster. However, Abaqus is limited in its geoscientific applications, whereas the open-source code ASPECT expands its applications in the realms of thermal convective flow. Despite the fundamental differences in these finite element codes, we see a reasonable agreement for the surface deformation and deformation rates. We demonstrate the use of AMR in ASPECT with laterally heterogeneous Earth models. This is a powerful tool when one wants to model several surface loads at different locations that change at different times.

6. Scaling and Material Averaging

In this section, we use the model setup as in Section 4.1 to perform scaling tests and compare the performance of key components of the geometric multigrid (GMG) and algebraic multigrid (AMG) solvers. In addition, we study the effects of different viscosity averaging schemes as they are required when using the GMG solver. Our goal is to demonstrate the performance advantages of GMG and to find the number of processors that can be used for a particular problem size, where the methods still scale.

The GMG method requires solving the same problems on coarser meshes but viscosity generally only exists on the finest mesh, therefore we need to transfer it from the fine mesh to the coarser meshes. ASPECT currently provides multiple options to achieve this. Here, we consider the two options that provide the most (harmonic average) or least (Q1 projection) amount of smoothing between the meshes. The first one is "harmonic average only viscosity," where viscosity on coarse cells is a piecewise constant per cell computed by the harmonic average of viscosity values at quadrature points on the finest cells. The second one is "project to Q1 only viscosity," which is a cell-wise projection from the viscosity on the finest cells from quadrature points to a Q1 polynomial space, which is then transferred to the coarse cells.

The total number of DoF is ~111 million and the Stokes system owns 26 million of them. Both GMG and AMG take about 40 GMRES (generalized minimal residual method) iterations to converge regardless of the number of cores and viscosity averaging methods. We observe that the AMG solver is not sensitive to different viscosity averaging schemes in these scaling tests, and we thus skip the results of the AMG solver without averaging viscosity. Table 5 show the runtime in time step 1 of the three important components of the solvers ("Setup," "Assembly," "Stokes solve"). Both GMG and AMG have similar scaling efficiency. The optimal scaling range is near 500 cores, leading to around 50,000 DoF per core.

The "Setup" part includes setting up all the sparsity patterns, distributing the DoF, and for GMG, it also includes initializing the data structures for the matrix-free multilevel transfer. Note that we only need this "Setup" part whenever the mesh is refined or coarsened. If a fixed mesh is used, everything in this part should be done in time step 0 only. GMG is about 1.7× faster than AMG for the setup, since it does not need to build any sparsity patterns for the Stokes equations. The "Assembly" part includes the runtime for all the matrix and vector assembly and preconditioner construction. For AMG, the matrices include the system matrix, preconditioner matrix, and preconditioner setup, while the GMG method only assembles the right-hand side of the linear system and computes necessary data on coarser levels. Here, GMG is at least 3.4× faster than AMG. Combining "Assembly" and "Stokes solve," GMG is at least 2.6× faster than AMG. Switching to harmonic averaging of the viscosity saves another 20% of the runtime (see Table 5). To work with AMR using GMG, one will have to consider the workload imbalance defined in Clevenger et al. (2020), which is caused by the unfair partition of the mesh. With 2,240 cores, this mesh produces an imbalance of 2.8 due to the heavy refinement at the surface. One can expect the GMG solver to be up to 2.8 times faster, if the mesh was globally refined like in the strong scaling results in Clevenger & Heister (2021).

Other important parts of the runtime include the assembly and solution of the compositional fields, mesh deformation, and temperature. More than 50% of the total runtime is spent in the assembly of the 10 compositional

Table 5
Runtime [s] of the Key Components in the GMG and AMG Solvers Using Q1 Projection and Harmonic Averaging for Viscosity

	Q1 projection of viscosity							
Number of processors	280		560		1,120		2,240	
Stokes DoFs/core	93,602		46,801		23,401		11,700	
Solver	GMG	AMG	GMG	AMG	GMG	AMG	GMG	AMG
Total	118.0	143.0	64.0	80.0	36.5	48.0	22.1	30.4
Setup	8.8	15.3	6.1	10.3	4.4	7.5	3.0	4.8
Assembly	4.5	15.1	2.4	8.5	1.3	5.0	0.7	3.4
Stokes Solve	6.7	14.3	3.6	7.5	2.4	4.7	1.8	3.5
Assembly + Stokes Solve	11.2	29.4	6.1	16.0	3.7	9.7	2.5	6.9
GMG speedup	2.6	–	2.6	–	2.6	–	2.8	–
	Harmonic averaging of viscosity							
Number of processors	280		560		1,120		2,240	
Stokes DoFs/core	93,602		46,801		23,401		11,700	
Solver	GMG	AMG	GMG	AMG	GMG	AMG	GMG	AMG
Total	106.0	136.0	59.0	75.0	34.2	46.0	20.5	30.7
Setup	9.0	15.5	6.0	10.2	4.4	7.4	3.0	5.3
Assembly	3.9	14.6	2.1	7.9	1.2	4.9	0.7	3.2
Stokes Solve	5.0	14.3	2.8	7.6	1.7	4.6	1.4	3.7
Assembly + Stokes Solve	8.9	28.9	4.9	15.5	2.9	9.5	2.1	6.9
GMG speedup	3.3	–	3.2	–	3.3	–	3.3	–

fields. Note that when the GMG solver is used, the matrix-free GMG method is used to solve for the mesh displacement, which is at least 3× faster than AMG and scales more efficiently, but it only takes about 1% of the total runtime. The temperature field takes about 5% of the total runtime to assemble and solve (the temperature equation is still solved although temperature is constant in our simulations). All the other parts not shown here contribute to less than 1% of the total runtime. Overall, using GMG can be at least 1.2× faster. Using GMG with harmonic average on 2,240 cores produces the greatest speedup, which is 1.5× faster than AMG in the total runtime in time step 1 as indicated in the first row in Table 5 for the harmonic averaging. Significantly, we observe almost no change in accuracy when varying between the AMG and GMG solvers, or viscosity averaging method (Table 6).

7. Conclusion

In this study, we benchmark a new viscoelastic solid Earth deformation model in ASPECT. ASPECT is a finite-element based code originally built for mantle convection studies. Unlike most other solid Earth deformation codes, it has all of the following advantages: it is open-source, built for parallel computing, has AMR capabilities, and can be extended by users. This new model can be used for regional modeling but not yet for global GIA studies, as it does not take into account gravity field changes induced by the deformation and does not solve for the gravitationally self-consistent redistribution of ocean water. We show the performance of Earth deformation in ASPECT and compare solutions to TABOO, a semianalytical code based on the normal mode method, and Abaqus, a commercial finite element code. We show that the maximum deformation and deformation rates in ASPECT agree within 2.6% for the average percentage difference with TABOO and

Table 6
Maximum Deformation After 5 years and Difference Relative to the TABOO Solution (−0.0305 m) for Abaqus and for 5 Different Combinations of the Stokes Solver Type and Material Averaging for ASPECT

Solution	Material averaging	Maximum deformation (m)	Difference relative to TABOO (%)
AMG	None	−0.0309442	+1.456
	Q1	−0.0308437	+1.127
	Harmonic	−0.0309272	+1.401
GMG	Q1	−0.0309081	+1.338
	Harmonic	−0.0309124	+1.352
Abaqus	–	−0.0301383	−1.186

Abaqus on glacial cycle and contemporary ice melt timescales. This gives confidence in the performance of our new solid Earth deformation model in ASPECT.

We show the performance of an adaptively refined mesh in ASPECT, which is a great advantage for solid Earth deformation modeling. Here, we model one cylindrical ice load. However, over a glacial cycle, and also for contemporary ice melt, surface loads increase or decrease at different rates and at different locations within the model domain. With the AMR capability and differently changing ice loads across the domain, we can model Earth deformation and speed up the computation considerably, saving computational resources by not requiring a highly refined mesh over regions where no large surface ice load changes occur. Furthermore, we show a good fit to Abaqus solutions comparing ice load-induced deformations above a laterally confined low-viscosity region, which supports the applicability of ASPECT for regional solid Earth deformation problems with lateral variations in Earth structure. Lastly, we report on the parallel scalability of the code, which is useful information for new users.

This benchmarked code can now be used to investigate the Earth deformation rates from past ice melt (ice age melting and long timescale) and contemporary ice melt (short timescale). This is especially interesting in areas of low-viscosity regions in the upper mantle beneath Antarctica and Greenland, where it is not fully understood how much ice age melting and contemporary ice melt contribute to modern geodetic measurements of Earth deformation (from GNSS). Or in other words, we can use ASPECT to estimate mantle viscosity from GNSS measurements in combination with an ice sheet evolution model over the last glacial cycle and observations of contemporary ice mass change.

Furthermore, ASPECT offers great flexibility to implement new code parts. We can for example, investigate the effect of nonlinear rheology on Earth deformation, such as time-dependent (e.g., transient) and stress-dependent viscosity (Adhikari et al., 2021; Blank et al., 2021; Lau et al., 2021), or the effect of anisotropic viscosity (Han & Wahr, 1997). This benchmark study is performed for a 3D box geometry, and developments are under way to solve for GIA in a 3D spherical geometry. Future development work will include adding self-gravitation to ASPECT, which already supports an option for variable gravity and solving the sea level equation, which involves implementing geoid changes, rotational feedback, shoreline migration, and associated ocean load redistributions. These developments will allow ASPECT to join a small suite of numerical 3D spherical GIA models.

Appendix A: Model Horizontal Dimension

In the benchmark test, the horizontal dimensions are 1,500 km for an ice load of 100 km radius. The lateral boundaries far from the load are free-slip boundaries (e.g., only tangential flow). In a spherical world these
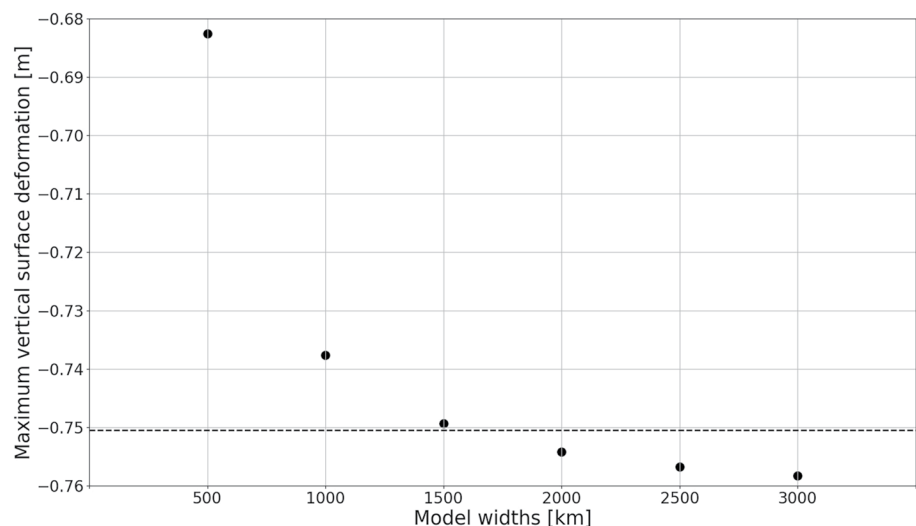
Figure A1. Maximum vertical surface deformation for models with different model widths (500–3,000 km) at 200 years in ASPECT (dots) and TABOO (dashed line).
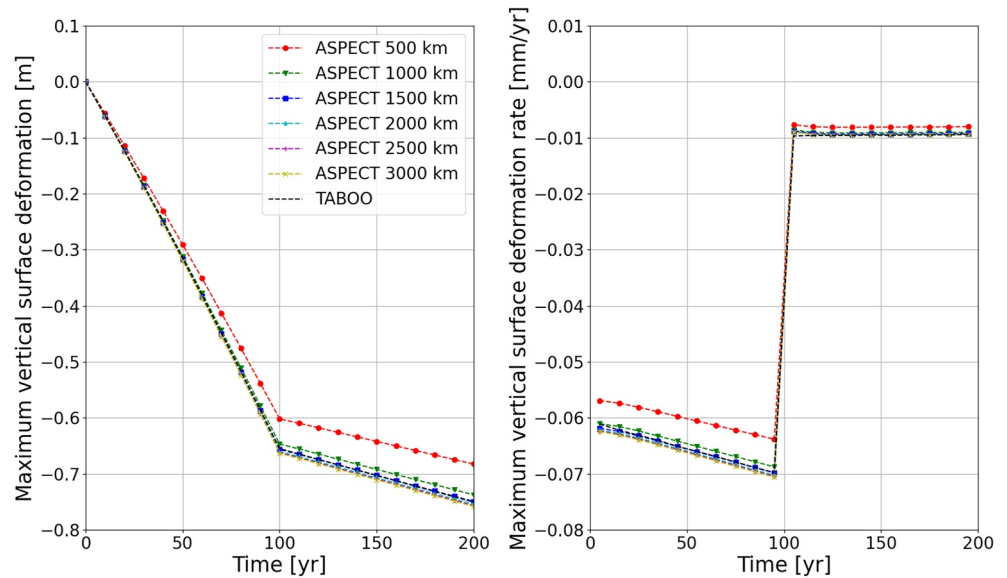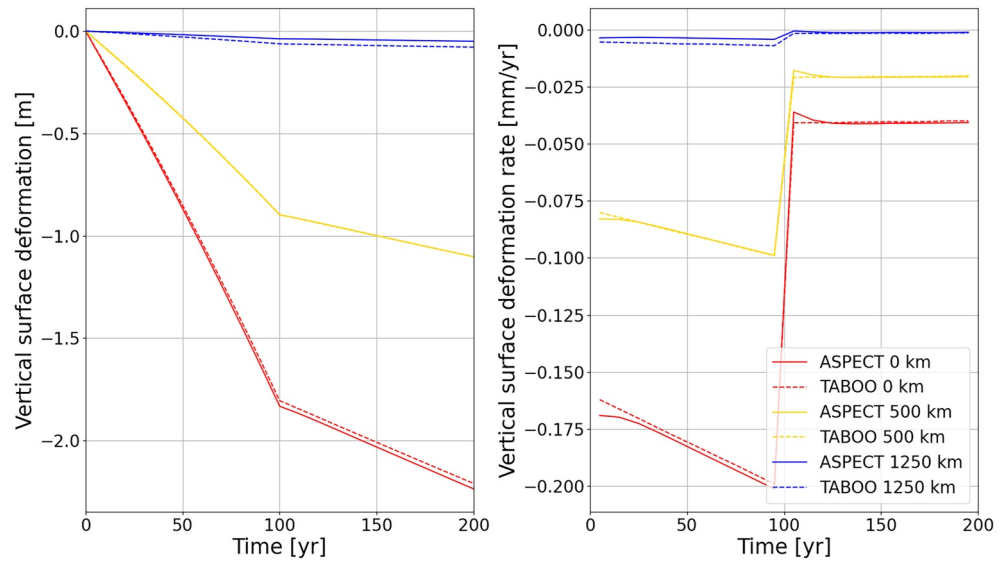
Figure A2. Maximum vertical surface deformation (left) and rate (right) for a model horizontal dimension of 500 km (red dots), 1,000 km (green triangles), 1,500 km (blue squares), 2,000 km (cyan stars), 2,500 km (magenta pluses), 3,000 km (yellow crosses), and TABOO (dashed black line).

boundaries do not exist. These boundaries can affect the material flow and thus the free surface deformation significantly. We wish to minimize the effect of the boundaries on the material flow, for an accurate representation of the surface deformation. Here, we demonstrate the effect the far lateral boundaries have by varying the model's horizontal dimension from 500 to 3,000 km (i.e., 5 times to 30 times the load radius).

The maximum vertical surface deformation for models with different model widths at 200 years decreases with an increase in model width (Figure A1). Convergence to a maximum vertical surface deformation is reached with an increase in model width. Thus, the lateral boundaries affect surface deformation, and thus material flow, less for a wider model, as expected. The model width is an important consideration for balancing between model accuracy and computational resources. We performed the model tests with a 1,500 km model width, resulting in a maximum deformation of −0.749 m, which is 1.2% off w.r.t. a model width of 3,000 km (Figure A2). Note that the model width has a large impact on the surface deformation when chosen too small (500 km width for a 100 km radius load). Model widths of 15 times the load radius (i.e., 1,500 km) used in this study, or larger, result in surface deformation and deformation rates within 1.4% of the solution using TABOO, and within 3.2% of the solution using TABOO for model widths of 10 times the load radius (i.e., 1,000 km) (Figure A2).

Appendix B: Sphericity and Self-Gravitation

We show the effect of the box model's nonspherical and nonself-gravitational features by applying wider surface loads. For regional GIA modeling, one needs to model not only the local ice load but also the surrounding ice masses because solid Earth deformation sensitivity stretches to distances away from the ice load. Amelung and Wolf (1994) showed the applicability of box models for regional studies. As ASPECT is nonspherical and nonself-gravitating, we test the effect of a wider surface load. Here, we increase the ice disc radius to 500 km and increase the model horizontal dimensions to 10,000 km (see Appendix A for the effect of lateral boundaries).

Figure B1. Maximum vertical surface deformation (left) and rate (right) for a load with 500 km radius as function of time for ASPECT (solid line) and TABOO (dashed line) at 0 km (red), 500 km (yellow), and 1,250 km (blue) distance from the load center.

From a first view, the deformation and deformation rates look similar between ASPECT and TABOO for the 500 km load radius (Figure B1). At a distance of 2.5 times the ice disc radius (i.e., 1,250 km), we see a similar difference between ASPECT and TABOO as for the 100 km radius ice disc at 250 km (Figures 3c and B1, blue lines). At the ice disc boundary, there is a better agreement for the 500 km disc radius (Figures 3c and B1, yellow lines), and underneath the center of the ice load the agreement slightly worsens for the 500 km radius ice disc (Figures 3c and B1, red lines). We see average percentage differences for the deformation and deformation rate well within 2.2% between the models underneath the load center and at 500 km distance (i.e., at the load boundary) (Table B1). Larger differences occur at 1,250 km distance (2.5 times the load radius) (Figure B1, blue lines), for example, we observe a ~30% average percentage difference in deformation rate between ASPECT and TABOO. However, the absolute rate is already remarkably small at this distance, with 0.001 mm/year at 200 years, which is 2.4% of the rate underneath the load center (Figure B1, right). Whereas the rate for the 100 km load radius was 0.0016 mm/yr at 250 km distance (also 2.5 times the load radius), which is 16% of the rate underneath the load center (Figure 3). On these larger scales, sphericity and self-gravitation seem to play

Table B1

Average Absolute and Percentage Difference of Vertical Surface Deformation and Deformation Rate at Different Distances From the Load Center Between ASPECT and TABOO for the Short Timescale Simulation for a Load Radius of 500 km

Distance from load center [km]	Deformation		Deformation rate	
	Avg. absolute difference [m]	Avg. percentage difference [%]	Avg. absolute difference [mm/yr]	Avg. percentage difference [%]
0	0.020	1.70	$1.90 \cdot 10^{-3}$	2.11
500	0.002	0.58	$5.31 \cdot 10^{-4}$	1.67
1,250	0.019	38.29	$1.44 \cdot 10^{-3}$	32.27

a smaller role close to the ice load and a larger but still minor role in the surface deformation and deformation rates further away from the ice load. This study agrees with findings from Amelung and Wolf (1994), Wu and Johnston (1998), and Ivins and James (1999). We show that the solid Earth deformation model in ASPECT is suitable for regional GIA modeling.

Appendix C: Model Density

In order to use ASPECT's adaptive mesh refinement (AMR) capabilities in combination with a free surface, we need to apply a constant density throughout the domain. With a laterally varying mesh, the vertically varying density is not equally represented laterally and free surface instabilities arise. Here, we show the effect of using a constant density as opposed to a density profile for ASPECT and TABOO.
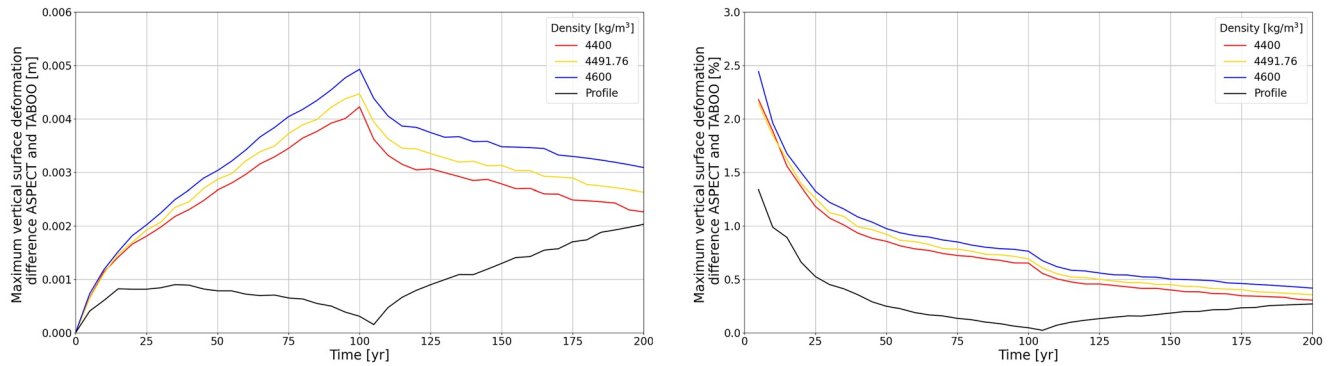
We set the constant density to the volume-averaged mantle density of the Earth model density profile, 4,491.76 kg/m^3. We run two more simulations with a constant density of 4,400 kg/m^3 and 4,600 kg/m^3 to show the effect of average density on the free surface deformation. In TABOO, we change the density of the preset Earth model in the source code. However, for the computation of the surface deformation based on load deformation coefficients (Spada, 2003), the average Earth density is required. In order to keep the reference average Earth density equal among runs with different constant density, we tune the core density accordingly in the source code.

The average percentage difference between using a density profile or a constant density is within 1.4% for the deformation and deformation rate at 0 km for ASPECT and within 2.0% for TABOO (Table C1). The average percentage difference is within 5.7% for both ASPECT and TABOO for distances from the load center of 0, 100, and 250 km (Table C1). The absolute difference in maximum vertical surface deformation between ASPECT and TABOO is slightly larger for the constant density cases (<0.005 m after 100 years or <1% percentage difference) than for the density profile (0.002 m after 200 years or <0.5% percentage difference) (Figure C1). Furthermore, we show that constant density variations give very similar surface deformation results compared to each other. Thus, the density value has a small effect on the surface deformation results. This test gives confidence in the performance of the models for either using a constant density or a density profile. Since density is not an important factor on the surface deformation results, we can confidently use the AMR in ASPECT.

Table C1
Average Percentage Difference of Vertical Surface Deformation and Deformation Rate at Different Distances From the Load Center Between the Density Profile and Constant Density of 4491.76 kg/m^3 for ASPECT and TABOO for the Short Timescale Simulation

Distance from load center [km]	ASPECT $\rho_{profile} - \rho_{constant}$		TABOO $\rho_{profile} - \rho_{constant}$	
	Deformation avg. percentage difference [%]	Deformation rate avg. percentage difference [%]	Deformation avg. percentage difference [%]	Deformation rate avg. percentage difference [%]
0	0.85	1.40	1.49	1.95
100	0.98	1.59	1.82	2.32
250	2.02	2.68	3.69	5.61

Figure C1. (a) Maximum vertical surface deformation absolute difference between ASPECT and TABOO and (b) percentage difference, as function of time for a constant density of 4,400 kg/m^3 (red), 4491.76 kg/m^3 (yellow), 4,600 kg/m^3 (blue), and the density profile as in the benchmark test (black).

Data Availability Statement

The open-source code ASPECT (v2.4.0) (Bangerth et al., 2022a, 2022b; Clevenger & Heister, 2021; Heister et al., 2017; Kronbichler et al., 2012; Rose et al., 2017) is available for download on GitHub (https://github.com/geodynamics/aspect/releases/tag/v2.4.0) or Zenodo (https://doi.org/10.5281/zenodo.6903424), along with the parameter and log files for the simulations in this study (https://doi.org/10.5281/zenodo.7334568). The open-source code TABOO (v1.1) is available for download on GitHub (https://github.com/danielemelini/TABOO). Abaqus 2019 is commercial licensed software and can be purchased through https://www.3ds.com/products-services/simulia/products/Abaqus/. In Figures 3, 4, and 7 the scientific cyclic color map romaO is used (Crameri, 2018).

References

Adhikari, S., Milne, G. A., Caron, L., Khan, S. A., Kjeldsen, K. K., Nilsson, J., et al. (2021). Decadal to centennial timescale mantle viscosity inferred from modern crustal uplift rates in Greenland. *Geophysical Research Letters*, *48*(19), e2021GL094040. https://doi.org/10.1029/2021GL094040

A, G., Wahr, J., & Zhong, S. (2013). Computations of the viscoelastic response of a 3-D compressible Earth to surface loading: An application to glacial isostatic adjustment in Antarctica and Canada. *Geophysical Journal International*, *192*(2), 557–572. https://doi.org/10.1093/gji/ggs030

Amelung, W., & Wolf, D. (1994). Viscoelastic perturbations of the Earth: Significance of the incremental gravitational force in models of glacial isostasy. *Geophysical Journal International*, *117*(3), 864–879. https://doi.org/10.1111/j.1365-246X.1994.tb02476.x

Arndt, D., Bangerth, W., Feder, M., Fehling, M., Gassmöller, R., Heister, T., et al. (2022). The deal.II library, version 9.4. *Journal of Numerical Mathematics*, *30*(3), 231–246. https://doi.org/10.1515/jnma-2022-0054

Austermann, J., Mitrovica, J. X., Huybers, P., & Rovere, A. (2017). Detection of a dynamic topography signal in last interglacial sea-level records. *Science Advances*, *3*(7), e1700457. https://doi.org/10.1126/sciadv.1700457

Bagge, M., Klemann, V., Steinberger, B., Latinović, M., & Thomas, M. (2021). Glacial-isostatic adjustment models using geodynamically constrained 3D Earth structures. *Geochemistry, Geophysics, Geosystems*, *22*(11), e2021GC009853. https://doi.org/10.1029/2021GC009853

Bangerth, W., Dannberg, J., Fraters, M., Gassmöller, R., Glerum, A., Heister, T., et al. (2022a). ASPECT: Advanced solver for problems in Earth's ConvecTion. *User Manual*. https://doi.org/10.6084/m9.figshare.4865333.v9

Bangerth, W., Dannberg, J., Fraters, M., Gassmöller, R., Glerum, A., Heister, T., et al. (2022b). ASPECT v2.4.0. *Zenodo*. https://doi.org/10.5281/zenodo.6903424

Barletta, V., Bevis, M., Smith, B., Wilson, T., Brown, A., Bordoni, A., et al. (2018). Observed rapid bedrock uplift in Amundsen Sea embayment promotes ice-sheet stability. *Science*, *360*(6395), 1335–1339. https://doi.org/10.1126/science.aao1447

Bevis, M., Wahr, J., Khan, S. A., Madsen, F. B., Brown, A., Willis, M., et al. (2012). Bedrock displacements in Greenland manifest ice mass variations, climate cycles and climate change. *Proceedings of the National Academy of Sciences of the United States of America*, *109*(30), 11944–11948. https://doi.org/10.1073/pnas.1204664109

Blank, B., Barletta, V., Hu, H., Pappa, F., & van der Wal, W. (2021). Effect of lateral and stress-dependent viscosity variations on GIA induced uplift rates in the Amundsen Sea embayment. *Geochemistry, Geophysics, Geosystems*, *22*(9), e2021GC009807. https://doi.org/10.1029/2021GC009807

Bradley, S. L., Hindmarsh, R. C. A., Whitehouse, P. L., Bentley, M. J., & King, M. A. (2015). Low post-glacial rebound rates in the Weddell Sea due to late Holocene ice-sheet readvance. *Earth and Planetary Science Letters*, *413*, 79–89. https://doi.org/10.1016/j.epsl.2014.12.039

Celli, N. L., Lebedev, S., Schaeffer, A. J., & Gaina, C. (2021). The tilted Iceland plume and its effect on the north Atlantic evolution and magmatism. *Earth and Planetary Science Letters*, *569*, 117048. https://doi.org/10.1016/j.epsl.2021.117048

Clevenger, T. C., & Heister, T. (2021). Comparison between algebraic and matrix-free geometric multigrid for a Stokes problem on an adaptive mesh with variable viscosity. *Numerical Linear Algebra with Applications*, *28*(5), e2375. https://doi.org/10.1002/nla.2375

Clevenger, T. C., Heister, T., Kanschat, G., & Kronbichler, M. (2020). A flexible, parallel, adaptive geometric multigrid method for FEM. *ACM Transactions on Mathematical Software*, *47*(1), 1–27. https://doi.org/10.1145/3425193

Crameri, F. (2018). Scientific colour maps. *Zenodo*. https://doi.org/10.5281/zenodo.1243862

Dannberg, J., & Gassmöller, R. (2018). Chemical trends in ocean islands explained by plume–slab interaction. *Proceedings of the National Academy of Sciences of the Unites States of America*, *115*(17), 4351–4356. https://doi.org/10.1073/pnas.1714125115

Dassault Systèmes (2019). Abaqus 2019. Retrieved from https://www.3ds.com/products-services/simulia/products/abaqus/

Glerum, A., Thieulot, C., Fraters, M., Blom, C., & Spakman, W. (2018). Nonlinear viscoplasticity in ASPECT: Benchmarking and applications to subduction. *Solid Earth*, *9*(2), 267–294. https://doi.org/10.5194/se-9-267-2018

Han, D., & Wahr, J. (1997). An analysis of anisotropic mantle viscosity and its possible effects on post-glacial rebound. *Physics of the Earth and Planetary Interiors*, *102*(1), 33–50. https://doi.org/10.1016/S0031-9201(96)03268-2

Heister, T., Dannberg, J., Gassmöller, R., & Bangerth, W. (2017). High accuracy mantle convection simulation through modern numerical methods—II: Realistic models and problems. *Geophysical Journal International*, *210*(2), 833–851. https://doi.org/10.1093/gji/ggx195

Helm, V., Humbert, A., & Miller, H. (2014). Elevation and elevation change of Greenland and Antarctica derived from CryoSat-2. *The Cryosphere*, *8*(4), 1539–1559. https://doi.org/10.5194/tc-8-1539-2014

Ivins, E. R., & James, T. S. (1999). Simple models for late Holocene and present-day Patagonian glacier fluctuations and predictions of a geodetically detectable isostatic response. *Geophysical Journal International*, *138*(3), 601–624. https://doi.org/10.1046/j.1365-246x.1999.00899.x

Ivins, E. R., James, T. S., Wahr, J., Schrama, E. J., Landerer, F. W., & Simon, K. M. (2013). Antarctic contribution to sea level rise observed by GRACE with improved GIA correction. *Journal of Geophysical Research: Solid Earth*, *118*(6), 3126–3141. https://doi.org/10.1002/jgrb.50208

Kaufmann, G., Wu, P., & Wolf, D. (1997). Some effects of lateral heterogeneities in the upper mantle on postglacial land uplift close to continental margins. *Geophysical Journal International*, *128*(1), 175–187. https://doi.org/10.1111/j.1365-246X.1997.tb04078.x

Khan, S. A., Sasgen, I., Bevis, M., van Dam, T., Bamber, J. L., Wahr, J., et al. (2016). Geodetic measurements reveal similarities between post–Last Glacial Maximum and present-day mass loss from the Greenland ice sheet. *Science Advances*, *2*(9). https://doi.org/10.1126/sciadv.1600931

Kronbichler, M., Heister, T., & Bangerth, W. (2012). High accuracy mantle convection simulation through modern numerical methods. *Geophysical Journal International*, *191*(1), 12–29. https://doi.org/10.1111/j.1365-246x.2012.05609.x

Latychev, K., Mitrovica, J. X., Tromp, J., Tamisiea, M. E., Komatitsch, D., & Christara, C. C. (2005). Glacial isostatic adjustment on 3-D Earth models: A finite-volume formulation. *Geophysical Journal International*, *161*(2), 421–444. https://doi.org/10.1111/j.1365-246X.2005.02536.x

Lau, H. C. P., Austermann, J., Holtzman, B. K., Havlin, C., Lloyd, A. J., Book, C., & Hopper, E. (2021). Frequency dependent mantle viscoelasticity via the complex viscosity: Cases from Antarctica. *Journal of Geophysical Research: Solid Earth*, *126*(11), e2021JB022622. https://doi.org/10.1029/2021JB022622

Li, T., Wu, P., Wang, H. S., Steffen, H., Khan, N. S., Engelhart, S. E., et al. (2020). Uncertainties of glacial isostatic adjustment model predictions in North America associated with 3D structure. *Geophysical Research Letters*, *47*(10), e2020GL087944. https://doi.org/10.1029/2020GL087944

Lloyd, A. J., Wiens, D. A., Zhu, H., Tromp, J., Nyblade, A. A., Aster, R. C., et al. (2020). Seismic structure of the Antarctic upper mantle imaged with adjoint tomography. *Journal of Geophysical Research: Solid Earth*, *125*(3). https://doi.org/10.1029/2019JB017823

Marsman, C. P., van der Wal, W., Riva, R. E. M., & Freymueller, J. T. (2021). The impact of a 3-D Earth structure on glacial isostatic adjustment in southeast Alaska following the little ice age. *Journal of Geophysical Research: Solid Earth*, *126*(12), e2021JB022312. https://doi.org/10.1029/2021JB022312

Martinec, Z., Klemann, V., van der Wal, W., Riva, R. E. M., Spada, G., Sun, Y., et al. (2018). A benchmark study of numerical implementations of the sea level equation in GIA modelling. *Geophysical Journal International*, *215*(1), 389–414. https://doi.org/10.1093/gji/ggy280

Martos, Y. M., Jordan, T. A., Catalán, M., Jordan, T. M., Bamber, J. L., & Vaughan, D. G. (2018). Geothermal heat flux reveals the Iceland hotspot track underneath Greenland. *Geophysical Research Letters*, *45*(16), 8214–8222. https://doi.org/10.1029/2018GL078289

Milne, G. A., Latychev, K., Schaeffer, A., Crowley, J. W., Lecavalier, B. S., & Audette, A. (2018). The influence of lateral Earth structure on glacial isostatic adjustment in Greenland. *Geophysical Journal International*, *214*(2), 1252–1266. https://doi.org/10.1093/gji/ggy189

Moresi, L., Dufour, F., & Mühlhaus, H.-B. (2003). A Lagrangian integration point finite element method for large deformation modeling of viscoelastic geomaterials. *Journal of Computational Physics*, *184*(2), 476–497. https://doi.org/10.1016/S0021-9991(02)00031-1

Nield, G. A., Barletta, V. R., Bordoni, A., King, M. A., Whitehouse, P. L., Clarke, P. J., et al. (2014). Rapid bedrock uplift in the Antarctic Peninsula explained by viscoelastic response to recent ice unloading. *Earth and Planetary Science Letters*, *397*, 32–41. https://doi.org/10.1016/j.epsl.2014.04.019

Pappa, F., Ebbing, J., Ferraccioli, F., & van der Wal, W. (2019). Modeling satellite gravity gradient data to derive density, temperature and viscosity structure of the Antarctic lithosphere. *Journal of Geophysical Research: Solid Earth*, *124*(11), 12053–12076. https://doi.org/10.1029/2019JB017997

Peltier, W. R. (1974). The impulse response of a Maxwell Earth. *Reviews of Geophysics*, *12*(4), 649–669. https://doi.org/10.1029/RG012i004p00649

Peltier, W. R. (1976). Glacial-isostatic adjustment—II. The inverse problem. *Geophysical Journal of the Royal Astronomical Society*, *46*(3), 669–706. https://doi.org/10.1111/j.1365-246X.1976.tb01253.x

Powell, E., Gomez, N., Hay, C., Latychev, K., & Mitrovica, J. X. (2020). Viscous effects in the solid Earth response to modern Antarctic ice mass flux: Implications for geodetic studies of WAIS Stability in a Warming World. *Journal of Climate*, *33*(2), 443–459. https://doi.org/10.1175/JCLI-D-19-0479.1

Root, B. C., Sebera, J., Szwillus, W., Thieulot, C., Martinec, Z., & Fullea, J. (2022). Benchmark forward gravity schemes: The gravity field of a realistic lithosphere model WINTERC-G. *Solid Earth*, *13*(5), 849–873. https://doi.org/10.5194/se-13-849-2022

Rose, I., Buffett, B., & Heister, T. (2017). Stability and accuracy of free surface time integration in viscous flows. *Physics of the Earth and Planetary Interiors*, *262*, 90–100. https://doi.org/10.1016/j.pepi.2016.11.007

Roy, K., & Peltier, W. (2018). Relative sea level in the Western Mediterranean basin: A regional test of the ICE-7G_NA (VM7) model and a constraint on late Holocene Antarctic deglaciation. *Quaternary Science Reviews*, *183*, 76–87. https://doi.org/10.1016/j.quascirev.2017.12.021

Sabadini, D. A. Y. R., & Portney, M. (1986). The effects of upper-mantle lateral heterogeneities on postglacial rebound. *Geophysical Research Letters*, *13*(4), 337–340. https://doi.org/10.1029/GL013i004p00337

Samrat, N. H., King, M. A., Watson, C., Hay, A., Barletta, V. R., & Bordoni, A. (2021). Upper mantle viscosity underneath northern Marguerite Bay, Antarctic Peninsula constrained by bedrock uplift and ice mass variability. *Geophysical Research Letters*, *48*(24), e2021GL097065. https://doi.org/10.1029/2021GL097065

Samrat, N. H., King, M. A., Watson, C., Hooper, A., Chen, X., Barletta, V. R., & Bordoni, A. (2020). Reduced ice mass loss and three-dimensional viscoelastic deformation in northern Antarctic Peninsula inferred from GPS. *Geophysical Journal International*, *222*(2), 1013–1022. https://doi.org/10.1093/gji/ggaa229

Sandiford, D., Brune, S., Glerum, A., Naliboff, J. B., & Whittaker, J. M. (2021). Kinematics of footwall exhumation at oceanic detachment faults: Solid-block rotation and apparent unbending. *Geochemistry, Geophysics, Geosystems*, *22*(4), e2021GC009681. https://doi.org/10.1029/2021GC009681

Scheinert, M., Engels, O., Schrama, E. J. O., van der Wal, W., & Horwath, M. (2021). Geodetic observations for constraining mantle processes in Antarctica. *Geological Society, London, Memoirs*, *56*(1), 295–313. https://doi.org/10.1144/M56-2021-22

Schotman, H. H. A., Wu, P., & Vermeersen, L. L. A. (2008). Regional perturbations in a global background model of glacial isostasy. *Physics of the Earth and Planetary Interiors*, *171*(1), 323–335. https://doi.org/10.1016/j.pepi.2008.02.010

Simpson, M. J. R., Wake, L., Milne, G. A., & Huybrechts, P. (2011). The influence of decadal-to millennial-scale ice mass changes on present-day vertical land motion in Greenland: Implications for the interpretation of GPS observations. *Journal of Geophysical Research*, *116*(B2), B02406. https://doi.org/10.1029/2010jb007776

Spada, G. (2003). The theory behind TABOO. Retrieved from https://github.com/danielemelini/TABOO/blob/master/DOC/TABOO-theory.pdf

Spada, G., Antonioli, A., Boschi, L., Brandi, V., Cianetti, S., Galvani, G., et al. (2003). TABOO user guide. Retrieved from https://github.com/danielemelini/TABOO/blob/master/DOC/TABOO_User_Guide.pdf

Spada, G., Barletta, V. R., Klemann, V., Riva, R. E. M., Martinec, Z., Gasperini, P., et al. (2011). A benchmark study for glacial isostatic adjustment codes. *Geophysical Journal International*, *185*(1), 106–132. https://doi.org/10.1111/j.1365-246X.2011.04952.x

Steffen, H., Kaufmann, G., & Wu, P. (2006). Three-dimensional finite-element modeling of the glacial isostatic adjustment in Fennoscandia. *Earth and Planetary Science Letters*, *250*(1), 358–375. https://doi.org/10.1016/j.epsl.2006.08.003

Steffen, R., Audet, P., & Lund, B. (2018). Weakened lithosphere beneath Greenland inferred from effective elastic thickness: A hot spot effect? *Geophysical Research Letters*, *45*(10), 4733–4742. https://doi.org/10.1029/2017GL076885

The IMBIE Team. (2018). Mass balance of the Antarctic ice sheet from 1992 to 2017. *Nature*, *558*(7709), 219–222. https://doi.org/10.1038/s41586-018-0179-y

The IMBIE Team. (2019). Mass balance of the Greenland ice sheet from 1992 to 2018. *Nature*, *579*(7798), 233–239. https://doi.org/10.1038/s41586-019-1855-2

van der Wal, W., Barnhoorn, A., Stocchi, P., Gradmann, S., Wu, P., Drury, M., & Vermeersen, B. (2013). Glacial isostatic adjustment model with composite 3-D Earth rheology for Fennoscandia. *Geophysical Journal International*, *194*(1), 61–77. https://doi.org/10.1093/gji/ggt099

van der Wal, W., Whitehouse, P. L., & Schrama, E. J. O. (2015). Effect of GIA models with 3D composite mantle viscosity on GRACE mass balance estimates for Antarctica. *Earth and Planetary Science Letters*, *414*, 134–143. https://doi.org/10.1016/j.epsl.2015.01.001

van Dam, T., Francis, O., Wahr, J., Khan, S. A., Bevis, M., & den Broeke, M. R. (2017). Using GPS and absolute gravity observations to separate the effects of present-day and Pleistocene ice-mass changes in South East Greenland. *Earth and Planetary Science Letters*, *459*, 127–135. https://doi.org/10.1016/j.epsl.2016.11.014

Vermeersen, L. L. A., & Sabadini, R. (1997). A new class of stratified viscoelastic models by analytical techniques. *Geophysical Journal International*, *129*(3), 531–570. https://doi.org/10.1111/j.1365-246X.1997.tb04492.x

Wan, J. X. W., Gomez, N., Latychev, K., & Han, H. K. (2022). Resolving glacial isostatic adjustment (GIA) in response to modern and future ice loss at marine grounding lines in West Antarctica. *The Cryosphere*, *16*(6), 2203–2223. https://doi.org/10.5194/tc-16-2203-2022

Weerdesteijn, M. F. M., Conrad, C. P., & Naliboff, J. B. (2022). Solid Earth uplift due to contemporary ice melt above low-viscosity regions of the upper mantle. *Geophysical Research Letters*, *49*(17), e2022GL099731. https://doi.org/10.1029/2022GL099731

Whitehouse, P. L. (2018). Glacial isostatic adjustment modelling: Historical perspectives, recent advances and future directions. *Earth Surface Dynamics*, *6*(2), 401–429. https://doi.org/10.5194/esurf-6-401-2018

Whitehouse, P. L., Bentley, M. J., Milne, G., King, M. A., & Thomas, I. D. (2012). A new glacial isostatic adjustment model for Antarctica: Calibrated and tested using observations of relative sea-level change and present-day uplift rates. *Geophysical Journal International*, *190*(3), 1464–1482. https://doi.org/10.1111/j.1365-246X.2012.05557.x

Wolstencroft, M., King, M. A., Whitehouse, P. L., Bentley, M. J., Nield, G. A., King, E. C., et al. (2015). Uplift rates from a new high-density GPS network in Palmer Land indicate significant late Holocene ice loss in the southwestern Weddell Sea. *Geophysical Journal International*, *203*(1), 737–754. https://doi.org/10.1093/gji/ggv327

Wu, P. (2004). Using commercial finite element packages for the study of Earth deformations, sea levels and the state of stress. *Geophysical Journal International*, *158*(2), 401–408. https://doi.org/10.1111/j.1365-246X.2004.02338.x

Wu, P., & Johnston, P. J. (1998). Validity of using flat-Earth finite element models in the study of postglacial rebound. In P. Wu (Ed.), *Dynamics of the ice age Earth: A modern perspective* (pp. 191–202). Trans Tech Publications Ltd.

Wu, P., Ni, Z., & Kaufmann, G. (1998). Postglacial rebound with lateral heterogeneities: From 2D to 3D modeling. In P. Wu (Ed.), *Dynamics of the ice age Earth: A modern perspective* (pp. 557–582). Trans Tech Publications Ltd.

Wu, P., & Peltier, W. R. (1982). Viscous gravitational relaxation. *Geophysical Journal International*, *70*(2), 435–485. https://doi.org/10.1111/j.1365-246X.1982.tb04976.x

Wu, P., Steffen, R., Steffen, H., & Lund, B. (2021). Glacial-isostatic adjustment models for earthquake triggering. In H. Steffen, O. Olesen, & R. Sutinen (Eds.), *Glacially-triggered faulting* (pp. 383–401). Cambridge University Press.

Yousefi, M., Milne, G. A., & Latychev, K. (2021). Glacial isostatic adjustment of the Pacific coast of North America: The influence of lateral Earth structure. *Geophysical Journal International*, *226*(1), 91–113. https://doi.org/10.1093/gji/ggab053

Zhao, C., King, M. A., Watson, C. S., Barletta, V. R., Bordoni, A., Dell, M., & Whitehouse, P. L. (2017). Rapid ice unloading in the Fleming Glacier region, southern Antarctic Peninsula and its effect on bedrock uplift rates. *Earth and Planetary Science Letters*, *473*, 164–176. https://doi.org/10.1016/j.epsl.2017.06.002

Zhong, S., Kang, K., A, G., & Qin, C. (2022). CitcomSVE: A three-dimensional finite element software package for modeling planetary mantle's viscoelastic deformation in response to surface and tidal loads. *Geochemistry, Geophysics, Geosystems*, *23*(10), e2022GC010359. https://doi.org/10.1029/2022GC010359

Zwinger, T., Nield, G. A., Ruokolainen, J., & King, M. A. (2020). A new open-source viscoelastic solid Earth deformation module implemented in Elmer (v8.4). *Geoscientific Model Development*, *13*(3), 1155–1164. https://doi.org/10.5194/gmd-13-1155-2020